Observed Structure and Propagation Characteristics of Tropical Summertime Synoptic Scale Disturbances

KAI-HON LAU

Atmospheric and Oceanic Sciences Program, Princeton University, Princeton, New Jersey

NGAR-CHEUNG LAU

Geophysical Fluid Dynamics Laboratory/NOAA, Princeton University, Princeton, New Jersey

(Manuscript received 29 December 1989, in final form 29 March 1990)

ABSTRACT

The three-dimensional structure and propagation characteristics of tropical synoptic scale transients during the northern summer are studied with twice daily ECMWF global gridded analyses for the 1980–1987 period. Regions of enhanced variability in relative vorticity at 850 mb are identified in the western Pacific, eastern Pacific, Bay of Bengal/northern India and eastern Atlantic/western Africa sectors. Dominant spectral peaks with time scales ranging from 3 to 8 days are noted in the power spectra for these locations.

The lag-correlation and regression statistics of tropical fluctuations with synoptic time scales are examined. Strong teleconnectivity and temporal coherence are found over all of the active sites with enhanced vorticity variance, as well as over the western Atlantic/Caribbean and the Indochinese Peninsula. These results indicate that a substantial amount of synoptic scale variability in the tropics is associated with propagating wavelike disturbances that remain coherent over several days. The disturbances in all active regions tend to travel west/northwestward. The eastern portion of each active site is characterized by rapid growth of the disturbances, whereas decay typically occurs in the western portion.

The transient behavior throughout the tropics is also investigated using Extended Empirical Orthogonal Function (EEOF) techniques. The sites of activity thus identified coincide with the locations inferred from the lag-correlation analyses. Using time series of the EEOF coefficients as a reference, the temporal evolution as well as the horizontal and vertical structure of the disturbances occurring in each active region are delineated by composites of selected meteorological variables. Well-defined changes in vorticity, vertical velocity, temperature and humidity at various tropospheric levels, as well as convective activity (deduced from the outgoing longwave radiation field), are discernible in the disturbances at various sites. Phase relationships among different variables are interpreted in terms of dynamical and physical processes operating within the disturbances. The horizontal phase tilt of the fluctuations and their positions relative to the ambient mean circulation suggest a tendency for kinetic energy transfer from the quasi-stationary flow to the transient eddies. Most of the findings reported here are in accord with previous investigations based on different analysis tools and more limited datasets.

Whereas considerable similarities are noted among disturbances occurring over various active maritime sites, the perturbations over central and western Africa exhibit structural characteristics that are unique to that region. Specifically, two propagation tracks are identified in the African sector. The northern track along southern Sahara consists mostly of eddies commonly found over arid zones, with ascent of warm and dry air over surface troughs. The southern track is collocated with the climatological rainfall maximum at about 10°N, and is associated with moist convective systems.

1. Introduction

The existence of westward propagating summertime disturbances in the northern tropics has been known for decades. Using surface data, Piersig (1936) and Regula (1936) were among the first to notice cyclonic circulation features traveling from western Africa towards the Atlantic, with a period of about four days and a wavelength of approximately 2000 km. Riehl (1954) described the characteristics of waves in the easterly trades over the Caribbean and coined the term "easterly waves." Most of the studies in the late 1960s and early 1970s were based on station radiosonde soundings and satellite cloud pictures. Carlson (1969a, 1969b) studied the synoptic evolution of wavelike summertime disturbances in Africa during 1967 and 1968, and tracked some cyclonic phenomena all the way to their decay in the Caribbean. He also reported that the wave troughs slope eastward with height in the lower troposphere, similar to the Caribbean easterly wave structure reported by Riehl (1954).

Burpee (1972, 1974) used spectral and composite methods to study the disturbances passing over several

Corresponding author address: Mr. Kai-Hon Lau, Program in Atmospheric and Oceanic Sciences, P.O. Box CN710, Sayre Hall, Princeton, N.J. 08544-0710.

African stations within 5°–33°N, and determined that the waves originate at 15°–30°E. He also found that an easterly wind maximum (now commonly known as the African Easterly Jet) develops along 15°N at about 700 mb in response to the strong temperature gradient between the Sahara and equatorial Africa/Gulf of Guinea. Strongest meridional wind perturbations were also found at 700 mb. The wave axes tilt eastward with height below this level of maximum wind, and tilt westward with height above it. Horizontally, a southwest to northeast phase tilt was found in the meridional wind perturbations between 5°–13°N, signifying a transfer of easterly momentum from the mean easterly jet to the wave disturbances. Burpee (1972) showed that the mean potential vorticity gradient along isentropic surfaces vanishes, thus, satisfying the necessary condition for instability of an internal baroclinic jet (Charney and Stern 1962). Burpee concluded that, in the region equatorward of the mean easterly jet, the horizontal and vertical wind shears are important energy sources for the African waves. Similar to the synoptic results shown in Figs. 2 and 4a of Carlson (1969b), Burpee (1974) also noticed that the African waves are associated with paired vortices. These cyclonic centers propagate westward along two east–west oriented tracks located at 15°–20°N and at 5°–10°N [see Burpee (1974), Fig. 10]. The northern track coincides with the semipermanent zone of minimum surface pressure, while the southern track lies near the seasonal mean rainfall maximum. The northern vortices have structures similar to those of desert thermal lows (with warm, dry air overlying the lower troughs), and the southern vortices are associated with moist convection.

With observations taken during the 1974 Global Atmospheric Research Program (GARP) Atlantic Tropical Experiment (GATE), Reed et al. (1977) and Norquist et al. (1977) used a composite method to investigate eight wave disturbances along 11°–12°N. These reference latitudes are located near the track of the southern vortices in the studies of Carlson (1969b) and Burpee (1974). Reed and collaborators reported that the wave troughs are associated with cold anomalies at lower levels, and warm anomalies at the upper levels. This finding is consistent with the earlier result of Carlson (1969a, 1969b) that the southern vortices are usually associated with moist convection. Reed et al. (1977) also noticed twin vorticity centers over western Africa, and suggested that the northern track dips southward along the monsoon trough over the ocean, and eventually merges with the southern track. Reed et al. (1977) also noted a sign reversal in absolute vorticity in the vicinity of the midtropospheric African jet. Thus, the flow field satisfies the necessary condition for barotropic instability of a zonal flow (Kuo 1949).

Over the equatorial western Pacific, Wallace and Chang (1969) and Wallace (1971) found low-level disturbances with periods of 4–5 days and wavelengths of 3000 km using spectral methods. Reed and Recker (1971) used a composite method to describe the vertical structure of the disturbances in that region. They found that the propagation speed and vertical wave structure change systematically from east to west. They attributed this to the longitudinal variation of the vertical shear in the ambient flow. The meridional wind perturbations tilt eastward with height at 170°E (where there is little shear in the mean wind), and westward at 135°E (where strong easterly shear exists between 900 and 125 mb).

The expanded observation platforms of the 1979 First GARP Global Experiment (FGGE) have facilitated further investigations into the behavior of tropical disturbances at locations where little or no station data were previously available. Nitta et al. (1985) and Nitta and Takayabu (1985) conducted a global survey of the tropical transients using the FGGE observations for July and August. They identified various regions with active summertime transient activities in the northern tropics by examining bandpass-filtered data for meridional wind and outgoing longwave radiation (OLR).

Nitta and Takayabu (1985) and Tai and Ogura (1987) used the FGGE analyses to show that there are west-northwestward propagating disturbances in the eastern tropical Pacific. Similar to the features observed over the Atlantic, the strongest geopotential height perturbations are found in the lower troposphere. They observed cold anomalies below 700 mb and stronger, warm anomalies at about 300 mb above the surface wave troughs. They found a westward tilt with height for the wave troughs in the eastern Pacific, similar to the vertical tilt of the Caribbean disturbances reported by Shapiro (1986). Tai and Ogura (1987) suggested only weak associations between the disturbances in the eastern Pacific and the Atlantic, contrary to the earlier finding by Simpson et al. (1969) that eastern Pacific cyclogenesis is significantly related to the African waves traveling across the Atlantic.

Since the FGGE year, global datasets have been analyzed and archived at various operational centers on a daily basis. The availability of these global analyses greatly expands our databases for empirical tropical studies. We are no longer confined to station data or observations taken within limited-area networks during intensive field experiments. Reed et al. (1988a, 1988b) studied the synoptic evolution of African wave disturbances appearing in the European Centre for Medium Range Weather Forecasts (ECMWF) analyses for the summer of 1985. They also found two preferred propagation tracks for African wave disturbances, and confirmed most of the earlier results. They used bandpass-filtered variance maps to locate the active transient regions, but noted that the spatial patterns are rather sensitive to the bandwidth of the filter chosen. In data-sparse areas, they showed that African wave features depicted by the ECMWF analyses are substantiated by independent satellite data. They concluded that the

ECMWF analyses are rather successful in depicting the African wave characteristics.

More recently, Liebmann and Hendon (1990) examined the ECMWF analyses of the near equatorial wind field during the September–December season. Their analysis was aimed primarily at the behavior of synoptic scale disturbances occurring within the 10°S–10°N zone. They reported the presence of westward propagating and equatorially trapped features in the highpass-filtered (periods less than six days) 850 mb meridional wind field that bear some resemblance to mixed Rossby–gravity waves. These near-equatorial fluctuations exhibit some notable differences from the transient disturbances located farther north and documented in various studies cited earlier in this section. For instance, the equatorial phenomena described by Liebmann and Hendon have distinctly longer wavelengths and faster phase speeds. Nonetheless, these authors pointed out the tendency for some of the equatorial disturbances to propagate meridionally out of the deep tropics, particularly in the western Pacific.

Up to the present, most of the empirical studies on tropical waves have been performed for the Africa/Atlantic sector. Much less attention has been given to synoptic scale tropical disturbances in other areas, particularly the western Pacific. The FGGE data have provided some valuable information for a particular year, but in view of the notable interannual variability of the tropical disturbances [see Wallace and Chang (1969), and Chang et al. (1970)], the climatological behavior of these transients needs to be ascertained using a larger dataset. With the accumulation of global analysis products over the past decade, we feel that this is an opportune time to document in detail the typical behavior of tropical and subtropical transient activities occurring in all parts of the globe. Specifically, we shall use an 8-year set of ECMWF gridded analyses to describe the properties of disturbances occurring within the 30°S–30°N zone during the northern summer. We shall determine the preferred geographical sites and propagation characteristics of these synoptic scale perturbations. We shall also document the evolution of the three-dimensional structure of disturbances found in the various active regions. By offering a comprehensive description of these disturbances, we wish to establish an updated observational basis for further investigations on their life cycles, their interaction with other circulation systems, and their role in the general circulation of the tropical atmosphere.

It was apparent to us in the early stage of our analysis that new diagnostic techniques had to be adopted to take full advantage of the increased data coverage. Through the study of midlatitude synoptic scale disturbances during recent years, numerous modern analysis techniques have already been developed. These tools have been demonstrated to work well in extracting information from long time-series of gridded datasets. Blackmon (1976) and Blackmon et al. (1977) identified elongated variance maxima of bandpass-filtered geopotential height field over the western and central midlatitude oceans as regions of strong baroclinic wave activity. Using one-point correlation maps of the height field, Blackmon et al. (1984a, 1984b) showed that the disturbances resemble zonally oriented wavetrains. On the basis of one-point correlation maps of the geopotential streamfunctions at various pressure levels, Wallace et al. (1988) illustrated the three-dimensional structure and propagation characteristics of the midlatitude cyclones in a few summary maps. We shall demonstrate that these procedures are equally applicable for describing the characteristics of the tropical transients with the presently available global analyses.

In the next section, the datasets used in this study will be described briefly. In section 3, the spatial distribution and spectral characteristics of the transients will be discussed with reference to the vorticity variations at the 850 mb level. The global characteristics of these transients as revealed by the lag-correlation methods (Wallace et al. 1988) will be presented in section 4. Another diagnostic tool that has found wide applications in the meteorological community is the empirical orthogonal function (EOF) technique (Kutzbach 1967). In section 5, an extended EOF analysis procedure will be described. It will be shown that the leading EOF modes in the tropical zone within the 3–10 day band are indeed the west/northwestward propagating disturbances noted in the previous sections. A composite method based on the EOF results will be outlined in section 6. Horizontal and vertical composites of different variables will then be used to show the spatial structure and time evolution of the tropical disturbances in various active regions. The relationships between the transients and the ambient quasi-stationary circulation will also be discussed. In the final section, we shall summarize the results, and discuss how some of the unresolved issues concerning the tropical transients may be addressed in the future.

2. Datasets

The primary dataset for this study consists of the twice daily (0000 UTC and 1200 UTC) operational analyses archived at ECMWF for June, July, and August (JJA) in 1980–1987. The data grid has a uniform horizontal resolution of 2.5° × 2.5°. Meteorological variables examined include the zonal and meridional wind, pressure velocity, temperature and geopotential height at seven standard pressure levels (100, 200, 300, 500, 700, 850 and 1000 mb). Specific humidity analyses are only available from 300 to 1000 mb. The data fields have been initialized by nonlinear normal mode schemes. Detailed descriptions of the dataset and the assimilation system can be found in Bengtsson et al. (1982) and Hollingsworth et al. (1986).

Twice daily gridded data for outgoing longwave radiation (OLR) observed by the United States National

Oceanic and Atmospheric Administration (NOAA) satellites for the 1980–1986 period are also used to investigate the relationships between tropical disturbances and convective activities. The horizontal resolution, 2.5° × 2.5°, is the same as the ECMWF analyses. The OLR data are available at 0900 and 2100 local times (LST).

Since the ECMWF first-guess fields are derived from numerical models, and spectral decomposition has been used in the archive process, it is prudent to ensure that our results are not artifacts of spurious model-dependent features or of spectral truncation errors. As an independent check of the ECMWF results, some of the diagnostics have been repeated on a set of gridded 850 mb wind analyses compiled by the Royal Observatory of Hong Kong (ROHK) for the period July 1981–December 1984. The latter dataset is produced by applying two passes of the Cressman successive correction scheme on station soundings, and the results are archived directly on a 5° × 5° data grid. The ROHK analyses cover the domain within 65°–165°E and 0°–65°N.

3. Spatial variability and spectral characteristics of vorticity perturbations

The sites of active tropical transients are illustrated in Fig. 1, which shows the JJA distribution of 850 mb root mean squared (rms) relative vorticity ζ. The background flow in which the transients are embedded may be inferred from the seasonally averaged winds at 850 mb, shown in Fig. 2. The choice of 850 mb ζ as the key meteorological variable in our study is largely based on findings in earlier works that maxima of this quantity are good indicators of the centers of tropical disturbances (Nitta et al. 1985; Reed et al. 1988a). Meridional wind was frequently used as the key parameter in earlier studies, when ζ was not readily available from individual station soundings. Geopotential height is not a suitable choice in the tropics because of its small spatial and temporal variation in the equatorial zone, and its strong latitudinal dependence farther poleward.

In Fig. 1, large rms values are indicative of regions with high amplitude or frequent transient disturbances. The general pattern in this figure is rather similar to the maps shown by Nitta et al. (1985). Comparing with the 850 mb JJA mean relative vorticity distribution (not shown), areas of active transient activities in the northern tropics often coincide with the mean relative vorticity maxima (i.e., mean summertime troughs). Note that all time scales from one day to a season are included here. Over the western Pacific, large rms values are located along a zone extending west-northwestward from about 5°N, 165°E towards the East and South China seas. This region of enhanced transients lies in the vicinity of the Asian monsoon trough, and is situated to the southwest of the mean southeasterly current in the estern Pacific (Fig. 2). Another region of large rms values is seen extending over the Bay of Bengal from the west coast of Burma to northwestern India. Enhanced variability is seen to occur over the desert area in northeastern Saudi Arabia. Large rms values are also found along the southern Sahara, stretching westward from about 15°N 40°E towards western Africa. West of 20°N, 5°W, this zone extends west-southwestward toward the eastern Atlantic Ocean and terminates at about 15°N, 30°W. This region is well known for its African easterly wave activity. In Fig. 2, the northwestern African sector is

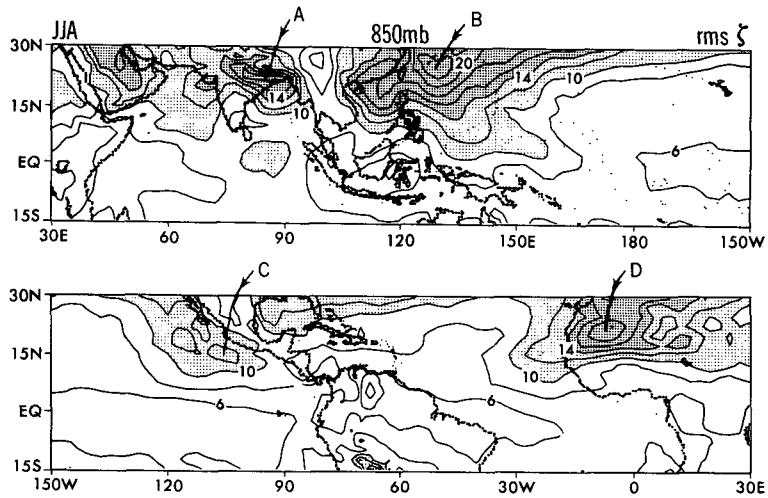

FIG. 1. Distribution of root-mean-squares of unfiltered vorticity fluctuations at 850 mb during the northern summer. Contour interval is 2×10^{-6} s^{-1}. Light stippling indicates values between 10×10^{-6} s^{-1} and 14×10^{-6} s^{-1}. Dense stippling indicates values greater than 14×10^{-6} s^{-1}.

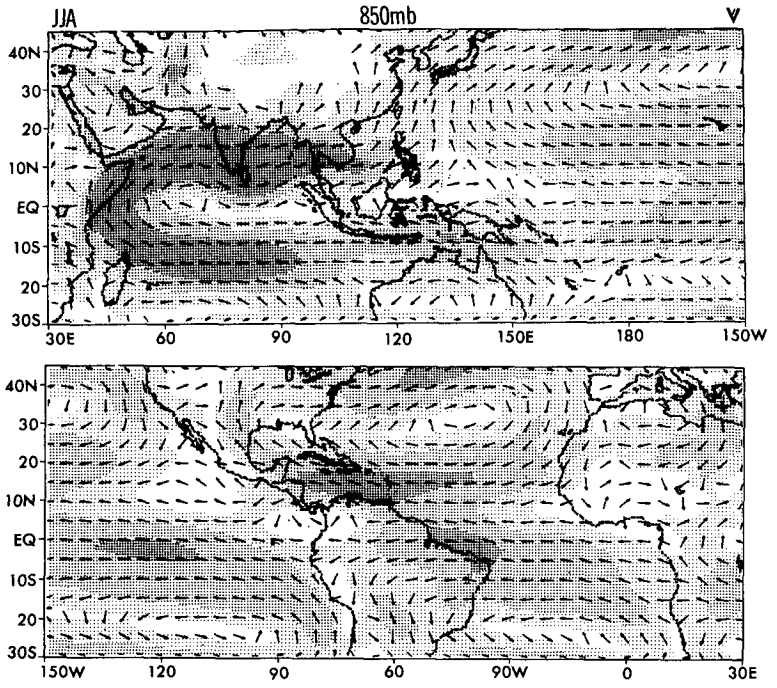

FIG. 2. Distribution of the climatological horizontal wind field at 850 mb during northern summer. Orientation of the arrows (with uniform length) indicates wind direction. Stippling indicates wind speed. Light stippling is used for values between 2–5 m s^{-1}, medium stippling for 5–8 m s^{-1}, and dense stippling for values larger than 8 m s^{-1}. Regions with mean wind less that 2 m s^{-1} are not stippled. A few arrows have been deleted in the Tibetan Plateau high terrain area for sake of clarity.

characterized by a relatively weak mean easterly current near 25°N. Not apparent in this figure is a local easterly maximum along 15°N at 600–700 mb [see Reed et al. (1977), Fig. 2a]. In the ECMWF data, the 700 mb easterly maximum (not shown) extends from central Africa at about 20°E towards the eastern Atlantic at about 35°W. Finally, a weaker maximum in rms values is found over the eastern Pacific in Fig. 1. This area extends northwestward from about 10°N, 90°W off the American coast. The mean wind in this region is very weak (Fig. 2).

To highlight the spectral characteristics of the tropical disturbances, power spectra of ζ at 850 mb have been computed for every gridpoint between 15°S and 30°N. These results indicate considerable variations in the dominant time scales of the fluctuations at different locations. In Fig. 3 the spectra are shown near four sample gridpoints for each of the following locations: (a) northeastern India, near 20°N, 85°E; (b) western Pacific, near 25°N, 130°E; (c) eastern Pacific, near 15°N, 105°W and (d) western Africa, near 20°N, 5°W. The chosen regions, as marked by A, B, C and D, respectively, in Fig. 1, coincide with local maxima in the distribution of rms ζ at 850 mb. Following Zangvil (1977), $\upsilon P(\upsilon)$ is plotted against $\ln(\upsilon)$ in Fig. 3, where υ is frequency and P is the power. This transformation takes into account the substantial degree of "redness" in most atmospheric spectra, such that a red noise spectrum with $P(\upsilon) = 1/\upsilon$ would appear as a horizontal line in the plot. Prominent departures from a horizontal line in Fig. 3 thus indicate the dominant time scales in vorticity fluctuations. This is also an area conserving transformation so that the total power at each gridpoint is still given by the area under the curve.

In northeastern India (Fig. 3a), we note a sharp spectral peak with a period of about 7–8 days, and a weaker peak at about two weeks. The latter may be related to the biweekly intraseasonal monsoon oscillations known to exist over this region (Hartmann and Michelsen 1989). From similar plots, we find that the 7–8 day peak is dominant and remains relatively sharp over the entire active region extending from the Bay of Bengal to northwestern India (Fig. 1). As shown in Fig. 3b, the dominant period over the western Pacific near 25°N 130°E is about 8–9 days. This characteristic time scale changes to about 5–7 days in regions farther east and farther south. The disturbances near 10°N 165°E are relatively weak and the dominant period further shortens to about 4–5 days, in accord with the earlier findings of Wallace and Chang (1969), Reed and Recker (1971), and others. In Fig. 3c, the power spectra near 15°N, 105°W show a relatively sharp peak at about 5–6 days, similar to results obtained by Nitta et al. (1985) and Tai and Ogura (1987). This time

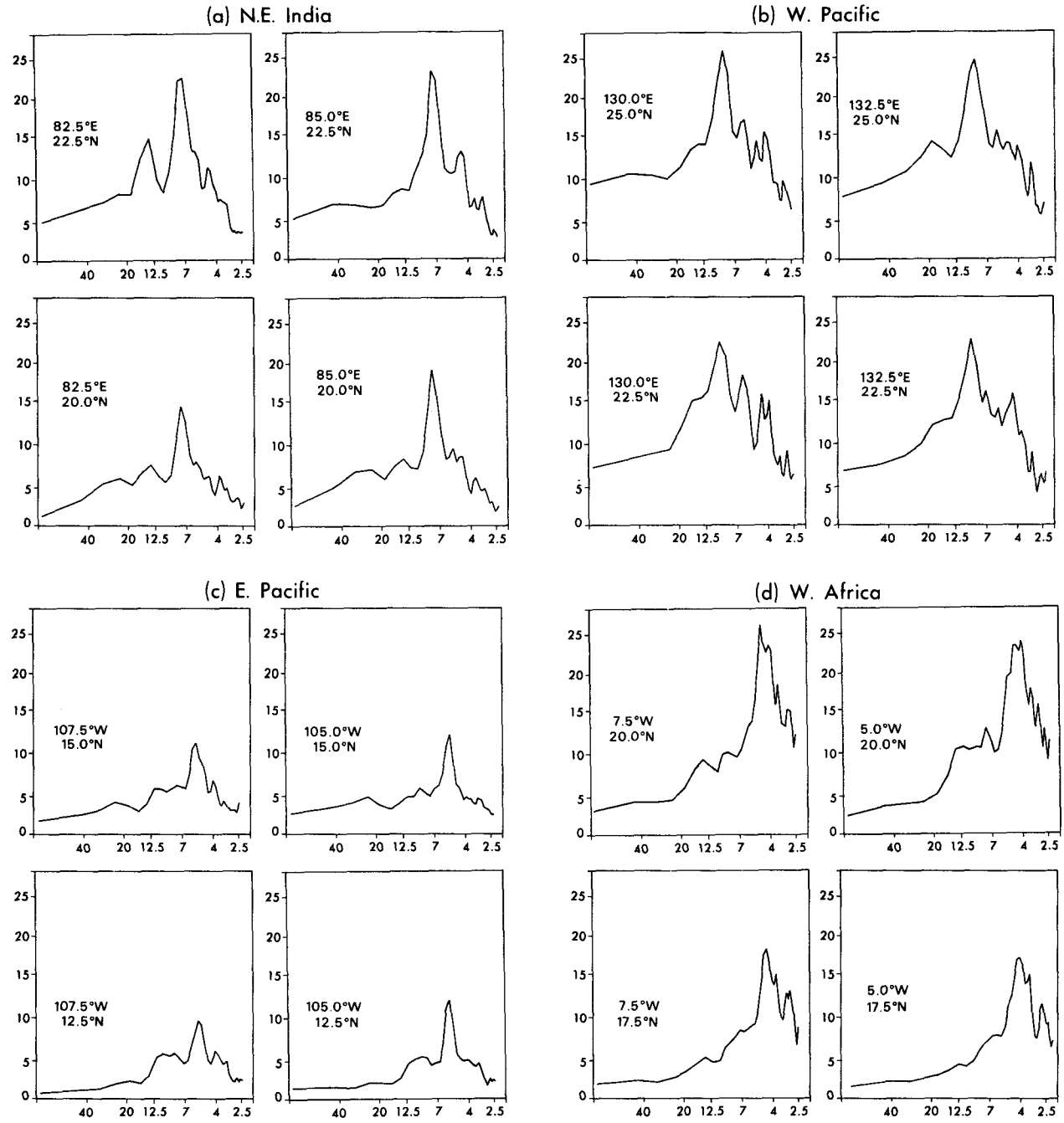

FIG. 3. Sample power spectra of relative vorticity, with $vP(v)$ plotted against $\ln(v)$, where v is the frequency and P is the power. The sites chosen correspond to maxima in the distribution of rms of vorticity in Fig. 1, and are marked as A, B, C, and D in that figure. These locations include (a) northeastern India, near 20°N, 85°E; (b) western Pacific, near 25°N, 130°E; (c) eastern Pacific, near 15°N, 105°W; and (d) western Africa, near 20°N, 5°W. Units are in day for the abscissa, and in 10^{-11} s^{-2} day^{-1} for the ordinate.

scale prevails throughout the region of enhanced rms in the eastern Pacific. Over western Africa, a 4–5 day peak stands out clearly in the spectra near 20°N, 5°W (Fig. 3d), and the dominant period shortens to about 3–4 days as we move southeastward to 15°N, 5°E.

The above results illustrate large variations of the dominant time scales over different regions of enhanced rms ζ. Similar conclusions were also drawn by Nitta et al. (1985). We also notice that the dominant period changes slowly, even along a given active zone in the western Pacific and western Africa, with a shorter period towards the east-southeastern end of each site. In

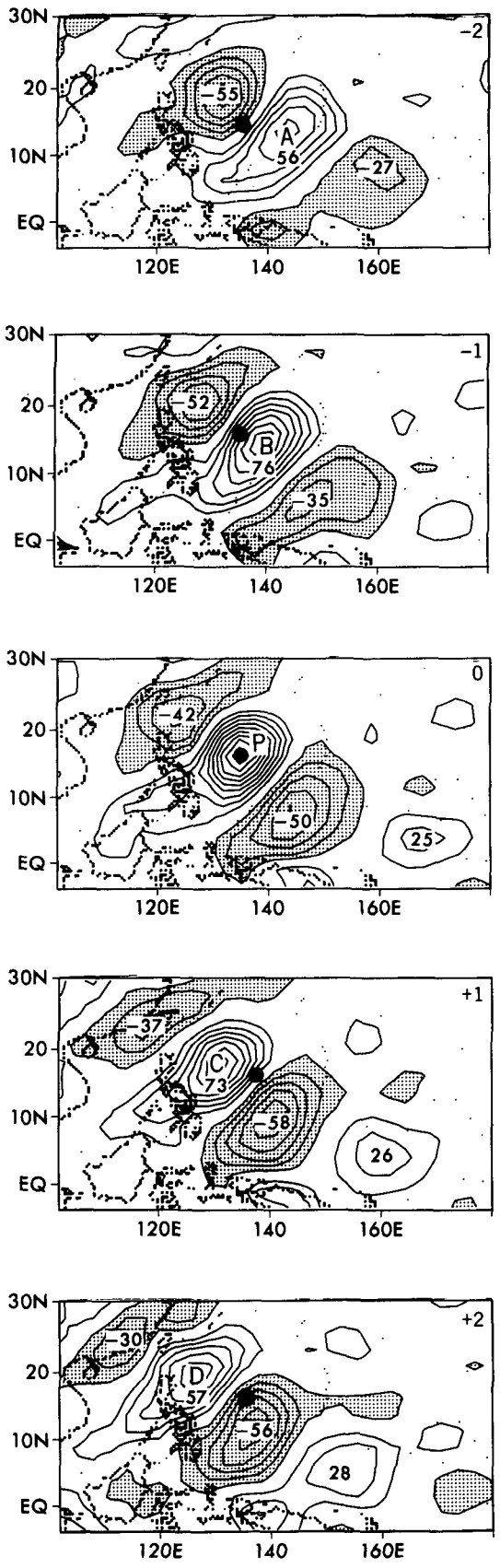

designing a suitable time filter, the considerable spatial variation of the wave periods dictates that the selected bandwidth should not be too narrow. Hence, a 61-point digital filter with half-power points at 2.5 and 12.5 days is chosen. This filter has a full response for periods from three to ten days. Unless otherwise specified, all parameters discussed hereafter are bandpass-filtered.

4. Lag-correlation analysis

Blackmon et al. (1984a, 1984b) and Wallace et al. (1988) have demonstrated that a substantial amount of information on midlatitude baroclinic waves in the Northern Hemisphere can be deduced from extratropical gridded analyses using lag-correlation techniques. On the basis of one-point correlation maps, Wallace et al. (1988) devised several anlaysis tools that are capable of delineating the vertical structure, time evolution, degree of waviness, phase propagation speed, temporal coherence and the growth/decay rates of the midlatitude cyclones. The same methods will be adopted in this section to describe the characteristics of transient phenomena occurring in the tropical zone.

a. One-point lag-correlation patterns

We begin by showing an example of a series of five one-point lag-correlation charts in Fig. 4. These are distributions of lag-correlation coefficients between the bandpass-filtered fluctuations in 850 mb ζ at the base point 15°N, 132.5°E and the corresponding fluctuations at all other gridpoints. The temporal lags used in this example range from −2 to +2 days. Here, negative (positive) lags refer to computations with the time series at individual gridpoints leading (lagging) the time series at the base point. Each panel in Fig. 4 indicates a wave-like structure with extrema of alternating polarity. Comparisons between the patterns in different panels reveal a systematic northwestward phase propagation. The average wavelength of the disturbances depicted in Fig. 4, as estimated from the distance between adjacent correlation centers with the same polarity, is approximately 2500 km. The typical period, given by twice the time interval between correlation patterns that are 180° out of phase with each other, is approximately six days (e.g., see panels corresponding to lags of −2 and +1 day). These estimates yield an average

FIG. 4. Distributions of lagged temporal correlation coefficients between bandpass-filtered 850 mb relative vorticity fluctuations at base point (15°N, 132.5°E) and the corresponding fluctuations at all other gridpoints. The temporal lag relative to the time series at the base point ranges from −2 to +2 days, and is indicated at the upper right-hand corner of the appropriate panel. The position of the base point is indicated by a solid dot in each panel. Extrema are expressed in percent. The contour interval is 10%, and values less than −10% are stippled. The zero contour has been omitted for sake of clarity.

propagation speed of 4.8 m s^{-1}. A characteristic southwest to northeast tilt of the elongated extrema is apparent in the patterns of Fig. 4. This eddy structure indicates an equatorward flux of easterly momentum (i.e., $\overline{u'v'} > 0$, where the overbar denotes the time mean, and the prime denotes deviations from the time mean). The placement of these disturbances in a region where the time-average easterly flow decreases equatorward (see Fig. 2) implies a downgradient momentum transport, and a local barotropic conversion from mean to eddy kinetic energy [i.e., $-\overline{u'v'}(\partial\bar{u}/\partial y) > 0$].

b. *Teleconnectivity*

The wavelike nature of the tropical disturbances may be further illustrated by a teleconnectivity analysis (Wallace and Gutzler 1981). The "teleconnectivity" for any point P is defined as the magnitude of the most negative correlation coefficient appearing in a simultaneous one-point correlation map corresponding to the base point P. A large teleconnectivity value for the point P implies that fluctuations at P are accompanied by strong fluctuations of the opposite polarity at other locations, and is hence indicative of the prevalence of wavelike phenomena in the vicinity of P.

Figure 5 shows the teleconnectivity pattern based on bandpass filtered ζ at 850 mb for the entire tropical belt. The values of teleconnectivity obtained here are comparable to those obtained by Wallace et al. (1988) for midlatitude baroclinic waves (see their Fig. 6). An area of strong teleconnectivity (larger than 0.4) is seen to extend west-northwestward from 5°N, 160°E towards southern China. This result suggests that a substantial fraction of the synoptic scale variability in the western Pacific may be attributable to wavelike disturbances. The region of enhanced teleconnectivity in the western Pacific coincides with the propagation path of the wavetrain shown in Fig. 4, and also with the axis of enhanced rms ζ (Fig. 1). Another region of strong teleconnectivity is found over the Bay of Bengal/northern India region. The most striking feature over the western hemisphere in Fig. 5 is a zone of moderate teleconnectivity (larger than 0.3) that spans across the Atlantic and central America from 20°E to 120°W. This feature is unique to the tropical Atlantic. No corresponding feature is found across the Pacific or Indian oceans. Within the western Africa/eastern Atlantic sector, a region of strong teleconnectivity along 15°–20°N is seen to extend from 5°W to 35°W. The teleconnectivity decreases in the mid-Atlantic and increases again in the Caribbean. The region of strong teleconnectivity over the Caribbean extends farther westward to the eastern Pacific, where weak wave activity has been reported by Nitta et al. (1985) and Tai and Ogura (1987). Strong teleconnectivity is also found near regions of high terrain such as the Tibetan Plateau, the Andes, and Iran. Since these mountains lie above the 850 mb level, it is not clear whether such strong teleconnectivity is indicative of real phenomena, or is merely an artifact of the extrapolations beneath nearby orographic features. In the present study, we shall not consider the behavior of lag-correlation statistics in the vicinity of these mountainous areas.

c. *Propagation vectors and temporal coherence*

The distributions of phase propagation vectors and temporal coherence for bandpass-filtered 850 mb ζ disturbances are displayed in Fig. 6 using arrows and stippling, respectively. The results shown here are based on one-point correlation maps similar to those in Fig. 4. For a series of lag-correlation charts corresponding

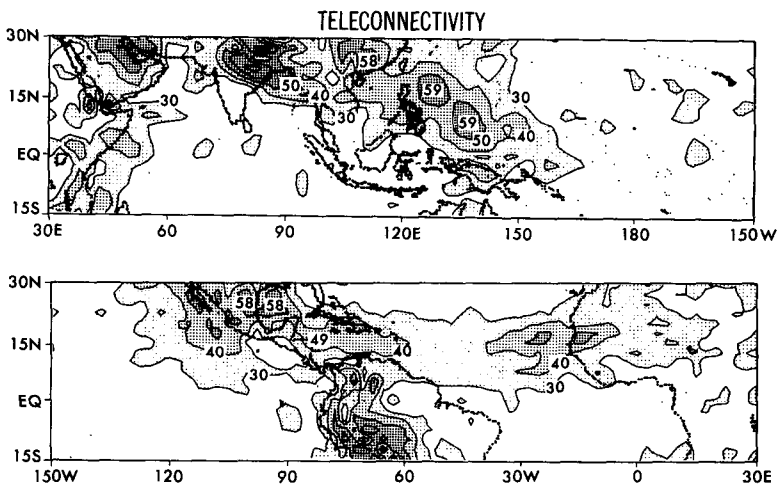

FIG. 5. Teleconnectivity map of the bandpass-filtered 850 mb relative vorticity field. Contour interval is 10%. Only values equal to or larger than 30% are contoured. The heaviest stippling corresponds to teleconnectivity values larger than 50%. See text for details of analysis procedure. Extrema and contour labels are expressed in percent.

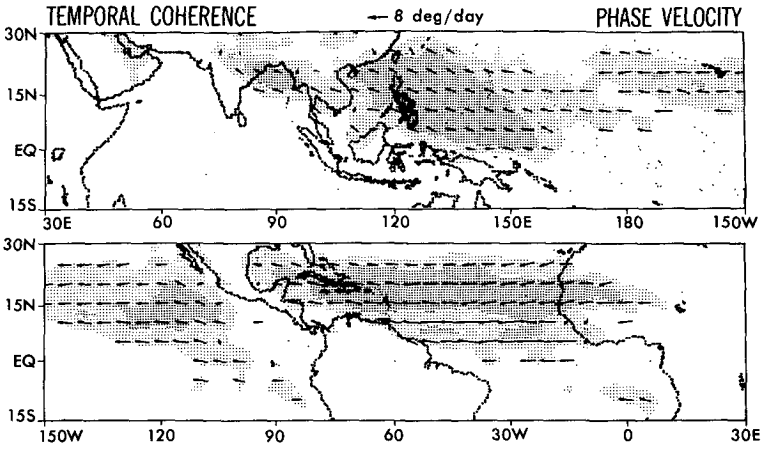

FIG. 6. Distrbution of phase propagation vector arrow for fluctuations in the bandpass-filtered 850 mb relative vorticity field. The stippling in this chart indicates those gridpoints that exhibit strong positive teleconnections at lags of −2 and +2 days. Light stippling denotes temporal coherence (average lagged-correlation) between 30% and 40%. Dense stippling denotes coherence exceeding 40%. Phase velocity vectors are drawn to scale and are plotted only at gridpoints with temporal coherence larger than 30%. See text for details of analysis procedure.

to the common base point P, the strongest positive correlation centers appearing in the panels for lags of −2 and +2 days have been identified and labeled as A and D, respectively (see example in Fig. 4). The line segments AP and PD represent the average spatial displacements of the disturbance center two days before and two days after its passage over P. The direction of the phase propagation vector at P may hence be inferred from the orientation of the line segment AD, and the magnitude of the propagation speed may be approximated by dividing the distance between A and D by the elapsed time interval (i.e., four days). Furthermore, the temporal coherence of the migratory signal for the base point P is defined as the average of the lagged correlation coefficients at points A and D. In contrast to teleconnectivity, which provides a measure of the waviness of a signal, the temporal coherence describes how well a migratory signal is maintained through its evolution in time. The coherence statistic makes no distinction between wavelike features (such as those highlighted in Fig. 4) and migratory monopolar vortices.

The pattern of arrows in Fig. 6 clearly shows a general west/northwestward propagation of the tropical transients. In the western Pacific, the average propagation speed of about 5 m s^{-1} in Fig. 6 is consistent with the estimation based on the characteristic wavelength and period deduced from Fig. 4. The temporal coherence attains maximum values along a belt extending from the equatorial Pacific to the south China coast. A region of strong temporal coherence (over 0.4) is also seen to extend from Burma towards northeast India. A longitudinally extended area of strong temporal coherence spans across the Atlantic from western Africa towards the Gulf of Mexico. The vectorial pattern in this sector indicates the prevalent propagation of transient wave activity from western Africa towards the Caribbean and the Gulf of Mexico. The temporal coherence drops significantly over continental Central America. Another zone of moderate temporal coherence reemerges in the eastern and central Pacific. Most of the sites mentioned here are characterized by enhanced ζ variability (Fig. 1) and teleconnectivity (Fig. 5).

Taking into account the time lag (between −2 and +2 days) used in computing the coherence statistics, the temporal coherence of tropical transients is comparable to that of midlatitude baroclinic waves [see Wallace et al. (1988), Fig. 8]. In Fig. 6, the temporal coherence over the southern tropical oceans and most land areas is generally under 30%, with the exception of western Africa and Indochina/northern India. We also note that the propagation speeds of the Atlantic and eastern Pacific disturbances (as shown by the length of the arrows) are faster than those found in the western Pacific and Indian regions. Assuming the horizontal scale of the disturbances in different regions to be similar, this implies a higher frequency (shorter period) for tropical waves in the western hemisphere, in agreement with the spectral results presented in section 3. The propagation speeds over the Atlantic Ocean also appear to vary significantly with latitude. The fastest propagation is found along 5°–10°N, and there is a gradual decrease in phase speed towards the north.

d. Growth/decay rates

Denoting the covariance and correlation coefficient between the bandpass-filtered ζ time series at any two points P and Q at lag $+n$ days as $\mathrm{cov}(P_0, Q_{+n})$ and

$\text{cor}(P_0, Q_{+n})$, respectively, we define the regression coefficient, $r_{+n}(P, Q)$, as

$$r_{+n}(P, Q) \equiv \frac{\text{cov}(P_0, Q_{+n})}{\sigma(P_0)} = \sigma(Q_{+n})\,\text{cor}(P_0, Q_{+n})$$

where $\sigma(P_0)$ and $\sigma(Q_{+n})$ are the standard deviations of the bandpass-filtered ζ at P and Q, respectively, calculated using the time series for periods that are shifted to each other by n days. With this definition in mind, the growth/decay rates of the disturbances can be estimated by the following procedure. From a series of one-point correlation maps corresponding to the base point P, the strongest positive correlation centers at lags of -1 and $+1$ day have been noted and labeled as B and C, respectively (see example in Fig. 4). The regression coefficients, $r_{-1}(P, B)$ and $r_{+1}(P, C)$, provide a measure of the amplitude of the vorticity fluctuations at B one day before, and at C one day after, the passage of a disturbance with an amplitude of one standard deviation over P. The growth/decay rate at P is then estimated as $[r_{+1}(P, C) - r_{-1}(P, B)]/(2 \text{ days})$.

In Fig. 7, the distribution of growth/decay rates thus obtained is shown. Growth areas are found in the upstream (eastern) regions, and decay in the downstream (western) regions of the known active sites. The most prominent feature is the large growth area over the western Pacific, which extends northwestward from around 0°N, 180°E. These disturbances cease to grow just off the south China coast, and strong decay rates are discernible along the coast and farther inland. For the Indian disturbances, growth is seen to prevail over the Bay of Bengal and the western portion of Indochina. In contrast to the western Pacific disturbances, the decay of these disturbances starts only after they cross the coast into the Indian subcontinent. Two regions of transient development are evident in central and western Africa. There is a northern growth region that extends continuously along the dry baroclinic zone near the Sahara at 20°N from 20°E to 5°W. A weaker southern growth region is found near the African coast of 10°N from 10°E to 20°W. This distribution is in agreement with earlier results by Carlson (1969b), Burpee (1974) and Reed et al. (1988a). Decay of the disturbances starts within continental western Africa, at 15°N, 5°–10°W, and extends west-southwestward towards South America. This pattern also agrees with earlier observations that the northern vortices decay earlier than those associated with the southern track (see Reed et al. 1977; Norquist et al. 1977). It is not evident from Fig. 7 that significant redevelopment occurs in the central Atlantic or the Caribbean, although scattered patches of growth areas can be found in the latter region. The western Mexico/eastern Pacific sector is characterized by another weak growth/decay dipole.

In summary, the spatial correspondence between the maxima in rms ζ (Fig. 1), teleconnectivity (Fig. 5), and temporal coherence (Fig. 6) indicates that a considerable amount of synoptic scale variability in the active tropical regions may be attributed to west-northwestward propagating wavelike disturbances that retain their identity for several days. We have also demonstrated that the lag-correlation statistics presented in this section provide considerably more in-

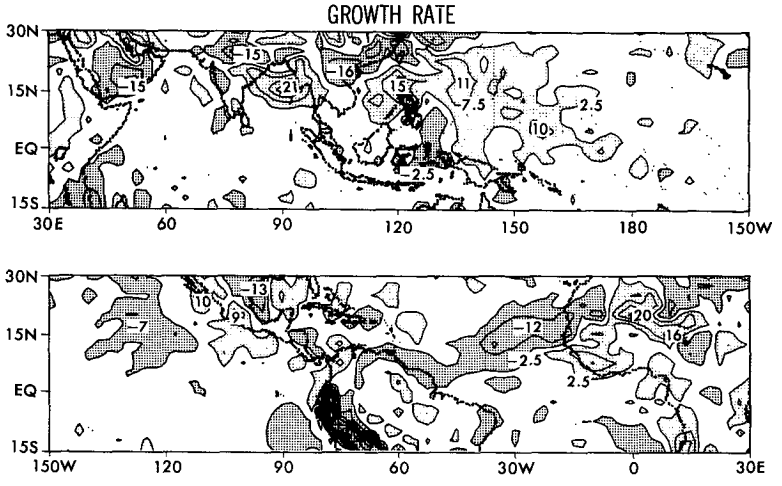

FIG. 7. Distribution of the growth or decay rate of fluctuations in the bandpass-filtered 850 mb relative vorticity field. Contour interval is 5×10^{-7} s^{-1} day^{-1}. Contour labels and extrema are expressed in units of 10^{-7} s^{-1} day^{-1}. Light stippling indicates positive vorticity tendencies exceeding 2.5×10^{-7} s^{-1} day^{-1} (growth). Dense stippling indicates negative tendencies less than -2.5×10^{-7} s^{-1} day^{-1} (decay). See text for details of analysis procedure.

formation on the transient behavior in the tropical atmosphere than the rms pattern alone. For instance, it is not evident in the unfiltered vorticity rms distribution of Fig. 1 that any organized transient activity exists in the central and eastern Atlantic, although the lag-correlation patterns in Figs. 5–7 as well as numerous previous synoptic studies have clearly demonstrated otherwise. Although the transient activities can also be identified with the rms distribution associated with vorticity time series filtered with narrow bandwidths, such rms fields are rather sensitive to small changes in the chosen frequency intervals (see Reed et al. 1988b, Fig. 4). Another case in point is the inference from the moderate teleconnectivity and coherent phase propagation over the Indochinese Peninsula that some of the disturbances in the Bengal region may be traced to remnants of transient activity originating from the western Pacific. This linkage between the fluctuations over the Pacific and those over the Bay of Bengal is hardly discernible from inspection of the rms distribution in Fig. 1.

Intercomparisons between the patterns in Figs. 5–7 reveal that, not withstanding the moderate temporal coherence spanning almost all the way across the tropical Pacific (Fig. 6), the weak teleconnectivity in the central Pacific (Fig. 5) and the tendency for the eastern Pacific disturbances to decay east of the date line (Fig. 7) do not suggest any strong relationship between wave activities in the eastern and western portions of the Pacific Basin. Finally, we also note that, with the exception of western Africa and northern India, the synoptic scale tropical disturbances are most active over maritime areas. Outside the Bay of Bengal, the Indian Ocean is notably void of any preferred path of propagation of organized synoptic scale activity.

5. Extended empirical orthogonal function analysis

Empirical orthogonal function (EOF) techniques have been used routinely in analyzing meteorological time series. Denoting observations taken at N stations (or gridpoints) at time t by an N-dimensional vector $\mathbf{X}(t)$, the conventional EOF analysis solves for the leading eigenvalues and corresponding eigenvectors of the $N \times N$ covariance matrix $\mathbf{X}\mathbf{X}^T$. The plots of leading eigenvectors (or EOFs) are indicative of the spatial structures of dominant modes that account for large fractions of the variance in the corresponding data field. For a concise description of the EOF analysis, the reader is referred to Kutzbach (1967).

Weare and Nasstrom (1982) introduced the extended EOF (i.e., EEOF) technique to include the temporal structure in the basic observation vectors by padding together data taken at adjacent times. For example, we may denote $\mathbf{Y}(t) = [\mathbf{X}(t), \mathbf{X}(t+1), \mathbf{X}(t+2)]$ as a $3N$-dimensional observation vector, with $\mathbf{X}(t+1)$ and $\mathbf{X}(t+2)$ lagging $\mathbf{X}(t)$ by one and two days, respectively. The variance maximization procedure for these extended vectors leads to the diagonalization and eigenvalue problem for the $3N \times 3N$ lagged-covariance matrix $\mathbf{Y}\mathbf{Y}^T$. Each of the resulting $3N$-dimensional eigenvectors may be partitioned into three individual N-dimensional fields, which may in turn be displayed in a series of three successive spatial patterns. These maps would delineate the space–time evolution of the dominant mode under consideration in three consecutive days. In both EOF and EEOF analyses, propagating modes usually appear as pairs of eigenvectors with comparable eigenvalues, and with spatial structures bearing a quadrature relationship with each other. The extended technique is more suitable in depicting propagating modes because the temporal evolutions are shown explicitly, and the propagation characteristics can be inferred readily from the spatial patterns associated with a single eigenvector.

The two basic constraints on EOFs (and EEOFs) are that each eigenvector must successively explain the maximum amount of the remaining variance, and that different eigenvectors and their temporal coefficients are orthogonal to each other. In many applications, EOFs tend to be influenced by the size and shape of the data domain. In particular, leading EOFs tend to show domain-wide structures with predictable anomaly distributions (Richman 1986). Moreover, North et al. (1982) showed that when two eigenvalues are nearly equal, sampling errors become very large, and that the corresponding EOFs may be intermixed. Richman (1986) gave an in-depth discussion of this subject, and showed that some of these problems may be resolved by rotating a few leading EOFs. Such rotations maximize local rather than global variance within the vector subspace spanned by the chosen leading EOFs. The new functions, hereafter referred to as rotated EOFs, are typically more localized, and correspond better with one-point lag-correlation patterns. Rotated EOFs are considered to be more suitable for analyzing localized fluctuations within a large domain. Rotation of EEOFs is analogous to rotation of EOFs, and the resultant vectors are hereafter denoted as REEOFs.

To describe the space–time evolution of the tropical transients, we have applied both EEOF and REEOF analyses on the bandpass-filtered summertime data for 850 mb ζ. Three temporal lags (at 0, 1, and 2 days) are used. Since the amplitudes of the disturbances exhibit considerable spatial variations (see section 4), the time-series at each gridpoint has been normalized to unit standard deviation. Thus, the EEOFs obtained are eigenvectors of the lag-correlation matrix. The first 20 EEOFs are then rotated. All calculations are done using a coarser $5° \times 5°$ grid to save computation time. The results presented in this section are considered to be robust in the sense that additional analyses with 1) meridional wind, 2) finer grid resolution: $2.5° \times 2.5°$, and 3) different number of temporal lags ranging from one (i.e., conventional EOF) to four, all yield similar leading eigenvector patterns.

Prior to a detailed eigen-analysis of the disturbances in different active regions, a preliminary global survey of the transients in the 40°S–40°N belt has been carried out. It is not possible to treat the entire tropical band as one single domain because of the large computer time and memory requirements. Instead, we have used 16 overlapping rectangular domains in the preliminary survey. Eight of these rectangles extended from 10°S to 40°N, and each rectangle spans over 90° of longitude. The starting points of these domains are 0°E, 45°E, 90°E, 135°E, 180°E, 135°W, 90°W and 45°W. The eight remaining domains extend from 40°S to 10°N, and have identical longitudinal divisions as the first set. Every gridpoint in the tropical zone is, therefore, covered in at least two adjacent domains. The overlapping boxes hence provide enough redundancy so that transient activities may be captured in at least one or two of these domains.

The global survey outlined above indicates that the only noteworthy feature in the Southern Hemisphere is the midlatitude cyclones found near the southern edges of the domains encompassing the 40°S–10°N zone (not shown). Organized tropical transient activities are found only in the Northern Hemisphere, and at the same geographical locations as the active sites inferred from the lag-correlation analysis in section 4. These regions include the western Pacific, Bay of Bengal/northeastern India, the eastern Pacific and the western Africa/Atlantic/Caribbean Sea sectors. On the basis of this preliminary survey, three areas have been chosen for more detailed analysis: the western Pacific and Indian domain (10°S–40°N 60°E–180°E), the Atlantic domain (15°S–30°N 90°W–30°E), and the eastern Pacific domain (10°S–40°N 165°W–75°W).

The leading REEOF in the western Pacific and Indian domain is shown in Fig. 8, and is hereafter referred to as WP1. The three panels in Fig. 8 show the evolution of WP1 within a 3-day time period, with the upper panel leading the middle and lower panels by one and two days, respectively. The WP1 mode explains 2.19% of the total variance. The second REEOF, WP2 (not shown), explains 2.11% of the total variance, and has a spatial structure nearly identical to WP1, except for a quadrature phase shift. The apparently small fraction of total variance explained by WP1 and WP2 (4.30%) must be viewed within the context of the localized nature of the disturbances in the large analysis domain chosen here. This percentage increases to 8.87% if we reduce the domain to 10°S–30°N 100°E–160°E, which is just enough to accommodate the spatial extent of WP1 and WP2. The larger domain has been chosen here so as to provide the REEOF procedure with sufficient flexibility in pinpointing the preferred sites of eddy activity. The phase relationship between WP1 and WP2, as well as the similarities in the their spatial structure and explained variances, imply that these two REEOFs essentially described the same propagating phenomenon. It is found that all leading

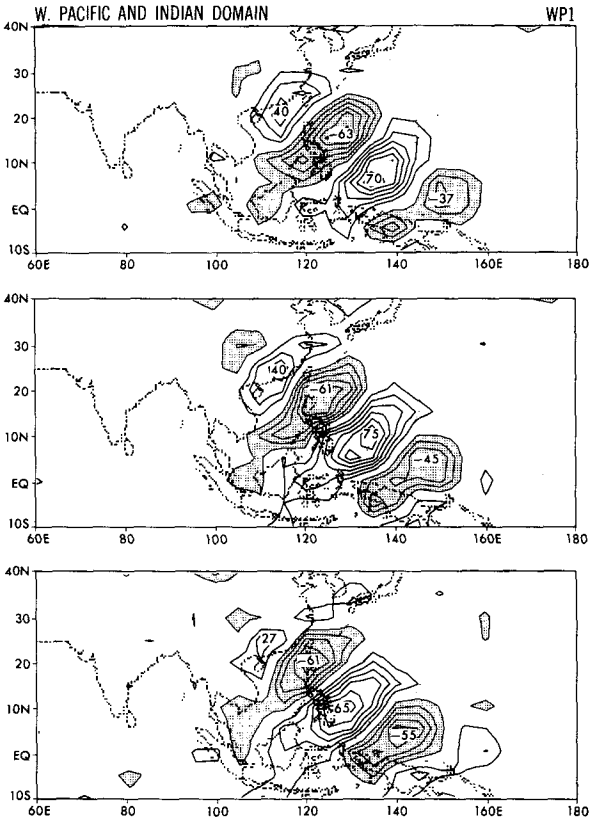

FIG. 8. Structure of the leading REEOF of bandpass-filtered vorticity fluctuations at 850 mb in the western Pacific and Indian domain (i.e., the WP1 mode). The panels show the time evolution of WP1 in three consecutive days, with the upper panel leading the middle and lower panels by one and two days, respectively. Extrema are expressed in percent. Contour interval is 10%. The zero contour has been omitted.

EEOFs and REEOFs of the bandpass-filtered dataset are paired in a similar manner, thus, indicating the prevalence of propagating disturbances in the chosen frequency band.

The structure of WP1 in Fig. 8 is very similar to the one-point lag-correlation maps in Fig. 4. Each panel is characterized by alternating positive and negative centers with a characteristic southwest to northeast tilt. Northwestward propagation is evident from the equatorial western Pacific to southeastern China. This track is coincident with enhanced rms of ζ, strong teleconnectivity, and high temporal coherence (see Figs. 1, 5, and 6).

The third and fourth REEOFs for the same domain are localized over southern Asia, and are denoted as the Indian modes; i.e., IN1 and IN2, respectively. They explain 1.54% and 1.46% of the total variance. The structure of IN1, shown in Fig. 9, consists of a northwestward propagating signal, traveling from the Indochinese Peninsula towards northwestern India. Lag-correlation maps with the base point at 20°N, 90°E (not shown) show similar horizontal structure and

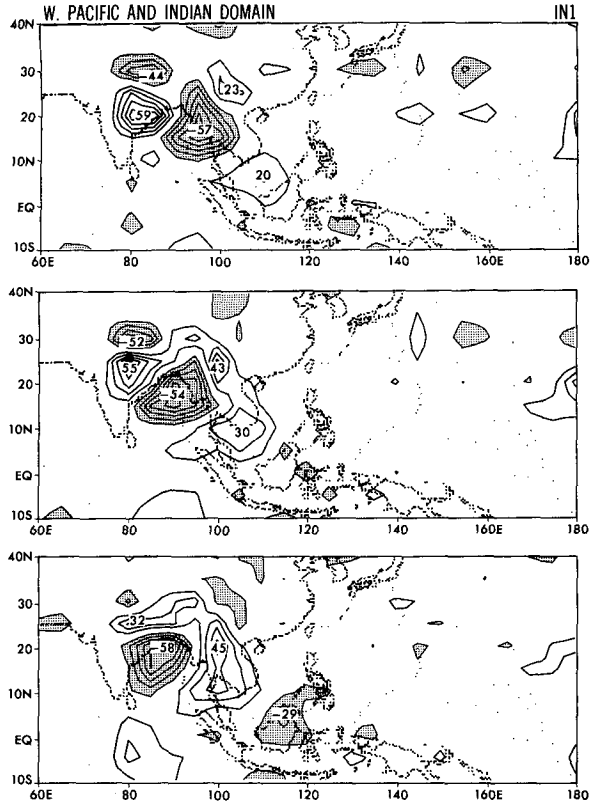

FIG. 9. Similar to Fig. 8, but for the third REEOF of the western Pacific and Indian domain (i.e., the IN1 mode).

propagation characteristics. In comparison with the western Pacific sector, the degree of waviness and eddy anisotropy are considerably weaker in the Bay of Bengal region.

The first pair of EEOFs for the Atlantic domain, denoted as AT1 and AT2, explain 2.63% and 2.60% of the total variance, respectively. The patterns for AT1, shown in Fig. 10, are indicative of disturbances propagating from near the Greenwich meridian towards the eastern Caribbean. A southwest to northeast phase tilt is evident to the south of 15°N, but no phase tilt is discernible to the north of this latitude. The structure is similar to the results obtained by Burpee (1974) and Reed et al. (1977) for the African easterly waves.

When compared with the unrotated eigenvector in Fig. 10, the REEOFs for the Atlantic domain (not shown) are more localized and bear a closer resemblance to one-point lag-correlation maps. Three pairs of REEOFs can be identified. One of these rotated modes corresponds to a northern track over continental west Africa; whereas the other two modes portray a southern track extending from Africa to eastern Atlantic, and a western track extending from the central Atlantic to the Caribbean Sea and the Gulf of Mexico. We have chosen to describe the transient behavior in the tropical Atlantic with EEOFs (instead of REEOFs) mainly because the former patterns are more consistent with earlier *synoptic* studies (e.g., Carlson 1969b; Reed et al. 1988a). These results indicate that the easterly waves are often associated with *concurrent* paired vortices in the low troposphere over western Africa. These vorticity centers tend to merge off the Atlantic coast, and subsequently migrate towards the Caribbean. It is, hence, more reasonable to represent the Atlantic disturbances using a single mode. In contrast, the disturbances in the Indian and the western Pacific regions appear to be two distinct entities and hence justify the representation using two separate pairs of REEOFs (Figs. 8 and 9).

Figure 11 shows the leading EEOF mode for the eastern Pacific domain, EP1. The first pair of EEOFs for this region explain 5.06% of the total variance. This mode illustrates the prevalence of northwestward propagating disturbances off the western seaboard of Central America. There is little evidence in Fig. 11 of any strong connection at the 850 mb level between disturbances over the eastern Pacific and those occurring east of Central America. Nevertheless, in analyzing a series of strong disturbances in this region during July 1975, Shapiro (1986) has shown evidence of vorticity propagation across Central America and the Yucatan Peninsula using a complex EOF analysis.

To ensure that the wavelike features found in this study are not merely artifacts of the spectral truncation

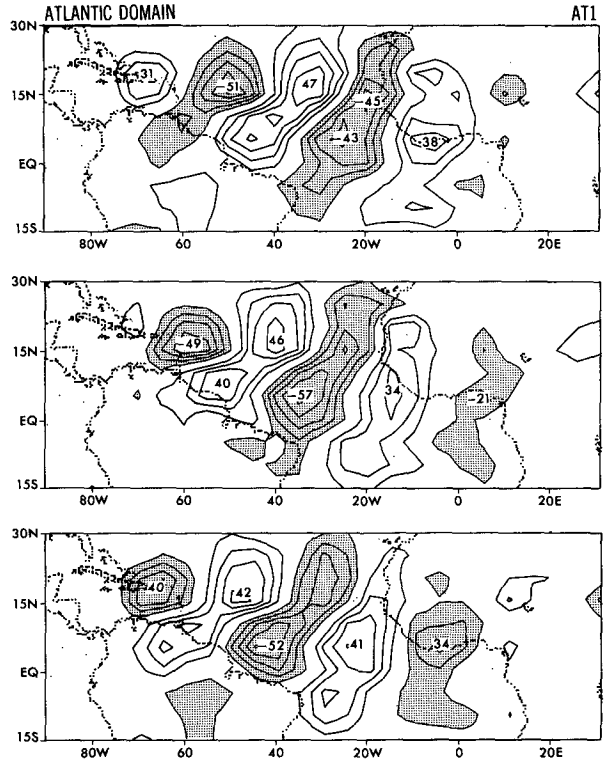

FIG. 10. Similar to Fig. 8, but for the leading EEOF of the Atlantic domain, (i.e., the AT1 mode).

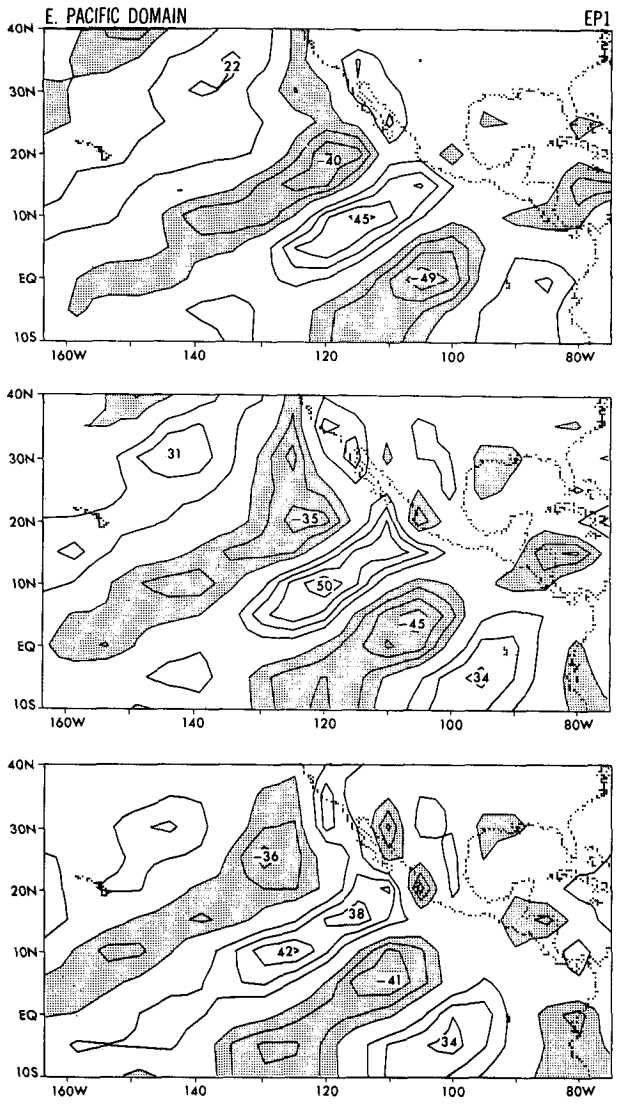

FIG. 11. Similar to Fig. 8, but for the leading EEOF of the eastern Pacific domain, (i.e., the EP1 mode).

used in archiving the ECMWF analyses, or the data assimilation procedures used in generating such data fields, one-point lag-correlation analyses have been performed with bandpass-filtered NOAA OLR data in the western Pacific. These computations yield patterns (not shown) which are nearly identical to the one-point lag-correlation charts in Fig. 4 based on the ECMWF vorticity analyses. The close correspondence between the results derived from these two independent datasets lends credence to the tropical circulation features appearing in the ECMWF analyses.

To assess the impact of time filtering on the structure of the principal of variability, we have applied the REEOF technique to the unfiltered ECMWF data for the western Pacific, and also to the unfiltered ζ time series derived from the wind analyses produced by the Royal Observatory of Hong Kong (ROHK). The first few EEOFs of both sets of analyses (not shown) are quasi-stationary on 5-day time scales. This result indicates that much of the variability in the tropics during the northern summer is associated with low-frequency fluctuations. Nevertheless, propagating modes resembling the spatial structure of WP1 are still found in the higher order modes for both sets of unfiltered analyses. Figure 12 shows the fourth REEOF mode of the unfiltered ROHK data. It is characterized by elongated positive and negative perturbations over the South and East China seas. The characteristic wavelength of ~2800 km is comparable to that of the WP1 mode. The axes of the extrema in Fig. 12 exhibit a more zonal orientation than the corresponding features in Fig. 8. This tendency towards more zonal tilts is common to other propagating modes based on unfiltered analyses. In summary, the existence of propagating modes in the REEOFs of unfiltered ROHK and ECMWF data demonstrates that the bandpass filtering is not the primary cause for the elongated wavelike disturbances described in this study. Furthermore, the similarity between the

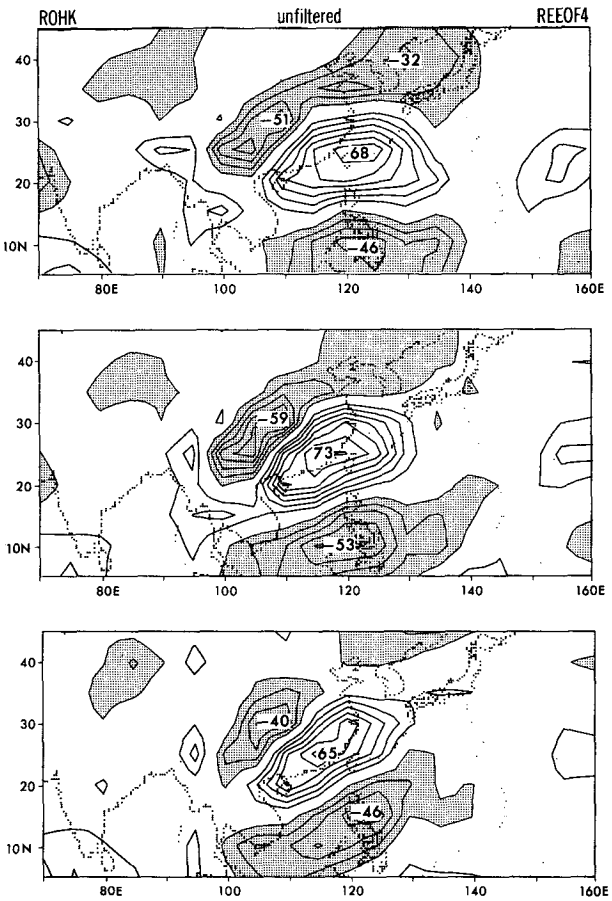

FIG. 12. Structure of the fourth REEOF of the unfiltered 850 mb relative vorticity fluctuations derived from the ROHK summertime wind analyses. Refer to the caption of Fig. 8 for other details.

ROHK and ECMWF results provides additional confirmation of the fidelity of the ECMWF dataset.

6. Composite analyses

In this section, the space–time evolution of selected meteorological variables associated with the disturbances in different active regions will be described using the composites constructed on the basis of the temporal EEOF/REEOF coefficients. The time coefficients of WP1 and WP2 for JJA 1980 are shown by the solid and dash curves in Fig. 13a, respectively. Each time series is normalized to have unit standard deviation for the 8-summer duration. It is evident from Fig. 13a that the two time series tend to be a quarter-cycle out of phase at most times. Denoting the time coefficients for WP1 and WP2 as $C_1(t)$ and $C_2(t)$, we define the amplitude $A(t)$ and the phase $\theta(t)$ for the WP mode as

$$A(t) = \left[\frac{C_1^2(t) + C_2^2(t)}{2}\right]^{1/2} \quad \text{and}$$

$$\theta(t) = \tan^{-1}\left[\frac{C_2(t)}{C_1(t)}\right].$$

The 1980 JJA segment of $A(t)$ and $\theta(t)$ for the WP mode are shown in Fig. 13b.

We shall describe the evolution of any variable (say, ζ) for each EEOF/REEOF mode by a sequence of 8 *phase composites* $\zeta_i = \zeta(\theta_i)$ of outstanding episodes for the corresponding mode. Here, ζ_i denotes the composite of ζ at phase $\theta = \theta_i$, where i varies from 1 to 8, and θ_i varies from 0° to 315° in intervals of 45°. We define an outstanding episode as a collection of consecutive time points through which i) the phase evolves at least one complete cycle, ii) the amplitude at each time point is larger than 0.75 standard deviation, and iii) the average amplitude for the consecutive time points is larger than 1 standard deviation. For each episode j satisfying the above criterion, we first obtain the eight values for $\zeta_{ij} = \zeta_j(\theta_i)$ by interpolation of the time series for ζ. The phase composite ζ_i for a given θ_i is then calculated by averaging the ζ_{ij}'s over all selected episodes (j's). Composite patterns based on different cutoff amplitudes are essentially similar to those shown here, indicating that our results are not crucially dependent on the choice of 0.75 standard deviation as the threshold.

For each EEOF/REEOF mode, an average amplitude and a mean period (time taken to complete one phase cycle) are calculated, first for each episode and then averaged over all episodes. After estimating the wavelength of the disturbances associated with WP, IN, AT and EP modes from the patterns in Figs. 8, 9, 10 and 11, respectively, the average phase speeds are also computed. Table 1 summarizes these characteristics for the four EEOF/REEOF modes discussed in the last section. The wavelengths of the four tropical modes are rather similar (from ~2800 km to ~3200 km), but the average period increases from 4.9 days for the AT mode to 6.8/6.9 days for the WP/IN modes. These estimates are consistent with the spectral and lag-correlation results obtained in sections 3 and 4. For each mode, the total number of days entering into the composite procedure are shown in the rightmost column of Table 1. This number is also expressed as a fraction (in percent) of the total number of days in the eight summer seasons (736). More days have been se-

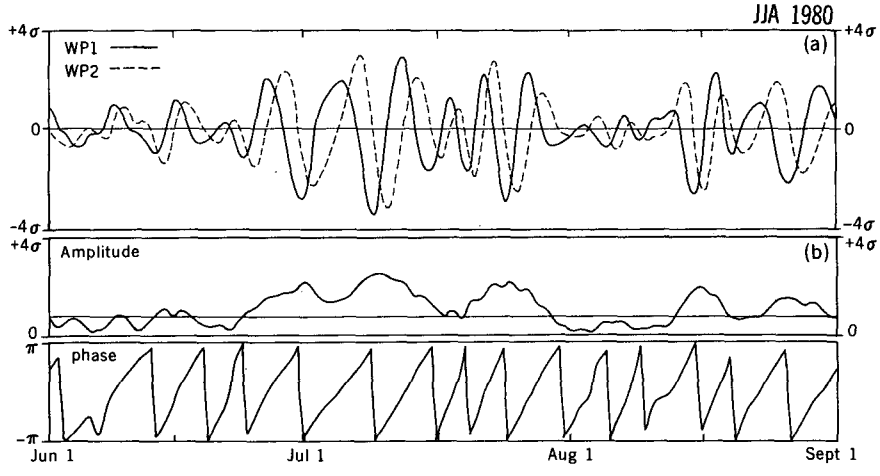

FIG. 13. (a) Time series of the coefficients for the two leading REEOFs of 850 mb bandpass-filtered vorticity fluctuations in the western Pacific and Indian domain (i.e., WP1 and WP2) during the summer of 1980. Each time series has been normalized so that the fluctuations for the entire eight-summer duration have unit standard deviation. (b) Time series of the amplitude and phase of the combined WP mode during the summer of 1980. The horizontal line in the amplitude plot marks the 0.75 standard deviation level, which has been chosen as the threshold for selecting outstanding episodes.

TABLE 1. Propagation characteristics of various tropical transient modes; the periods and amplitudes for the modes are given in (mean ± 1 standard deviation) as estimated from all the selected episodes. See text for details of the averaging procedure.

Mode	Period (day)	Wavelength (km)	Phase speed ($m\ s^{-1}$)	Amplitude (σ)	Number of days selected
WP	6.8 ± 1.1	~2800	4.8	1.55 ± 0.46	393 (53%)
IN	6.9 ± 1.1	~3000	5.0	1.47 ± 0.42	395 (54%)
AT	4.9 ± 1.0	~3200	7.6	1.31 ± 0.33	484 (66%)
EP	5.6 ± 1.2	~2800	5.8	1.39 ± 0.38	544 (74%)

lected for the unrotated EEOF modes (AT and EP) than the REEOF modes (WP and IN).

In the following subsections, we shall use the phase composites to show the three-dimensional structure of selected variables for the WP, IN, and AT modes. The WP mode will be discussed in greater detail, partly as an illustration of the composite method, and partly because the structure of synoptic scale disturbances in this region is not as well documented as at the other sites. To limit the length of this paper, the transient disturbances associated with the EP mode will not be discussed. Their structure is rather similar to the WP mode between 5°–15°N, and their amplitude are comparatively weaker.

a. Western Pacific mode

Figure 14a–d show four OLR composites of the WP mode at phases 0°, 90°, 180° and 270°, respectively. They are characterized by alternating bands of positive and negative OLR fluctuations extending across the East and South China seas. It is evident that the perturbations propagate northwestward. The fluctuations are rather weak and disorganized in the southern portion of the propagation path, but become much more organized as they travel towards the south China coast. As in the vorticity patterns shown in Fig. 8, the OLR perturbations also have pronounced southwest to northeast phase tilts. The prominent OLR signatures in the composites indicate that the WP disturbances are closely associated with well-defined convective activity.

The horizontal and vertical structures of different variables associated with the WP mode are presented in Figs. 15 and 16, respectively. All composites shown here correspond to the same phase (90°) as the OLR composite in Fig. 14b. The variables mapped in Fig. 15 include (a) 500 mb ζ, (b) 850 mb ζ, (c) 850 mb geopotential height, (d) 300 mb pressure velocity, ω, (e) 300 mb temperature and (f) 850 mb specific humidity. The vertical cross-sections for (a) relative vorticity, (b) geopotential height, (c) pressure velocity, (d) temperature and (e) specific humidity are displayed in Fig. 16. The abscissa in the latter plots corresponds to the propagation path of the most active disturbances, and extends southeastward from south China (27.5°N, 110°E) in the extreme left to the western equatorial Pacific (2.5°N, 142.5°E) in the extreme right (see bold line in Fig. 14b).

Comparison between the horizontal composite pattern for 850 mb ζ (Fig. 15b) and OLR (Fig. 14b) reveals that the phase relation between these two variables changes along the propagation path. In the equatorial region, negative OLR perturbations lead positive ζ fluctuations by as much as a quarter wavelength, indicating the convective activity tends to occur downstream of the wave troughs. This result is consistent with earlier findings [Reed and Recker (1971) and others] that the heaviest precipitation usually precedes the arrival of wave troughs over the equatorial western Pacific. Beyond the Philippine Islands in the northwestern part of the propagation path, negative OLR perturbations almost coincide with positive ζ centers, indicating that the strongest convective activity lies almost directly above the lower level troughs.

The vertical section of ζ (Fig. 16a) indicates a strong northwestward tilt with height over the equatorial ocean where initial wave growth is detected (see Fig. 4). This vertical tilt decreases gradually as we scan the figure from right to left, until there is almost no vertical tilt as the disturbances approach the south China coast. Vorticity perturbations are strongest at 850 mb. The fluctuation amplitude decreases most rapidly with height near the initial growth region (5°N, 160°E), where earlier studies by Yanai et al. (1968) and Wallace and Chang (1969) indicate that the transients tend to be confined below 500 mb.

The geopotential height composites in Figs. 15c and 16b show an expected out-of-phase relation with ζ. It is evident that geopotential height is not a good indicator for transient activities in the tropics. No height perturbation is discernible in the equatorial region, whereas the height signal in the subtropics is over emphasized.

Since the pressure velocity is rather sensitive to details in the data assimilation procedures and in model physics, the composite patterns for this field must be examined with due caution. The horizontal composite pattern for 300 mb ω (Fig. 15d) indicates rather weak organization of this field in the equatorial region, where initial growth is detected. The ω perturbations appear to be much better organized in the northwestern portion of the track, after substantial growth of the disturbances has occurred. It is seen from Fig. 16c that

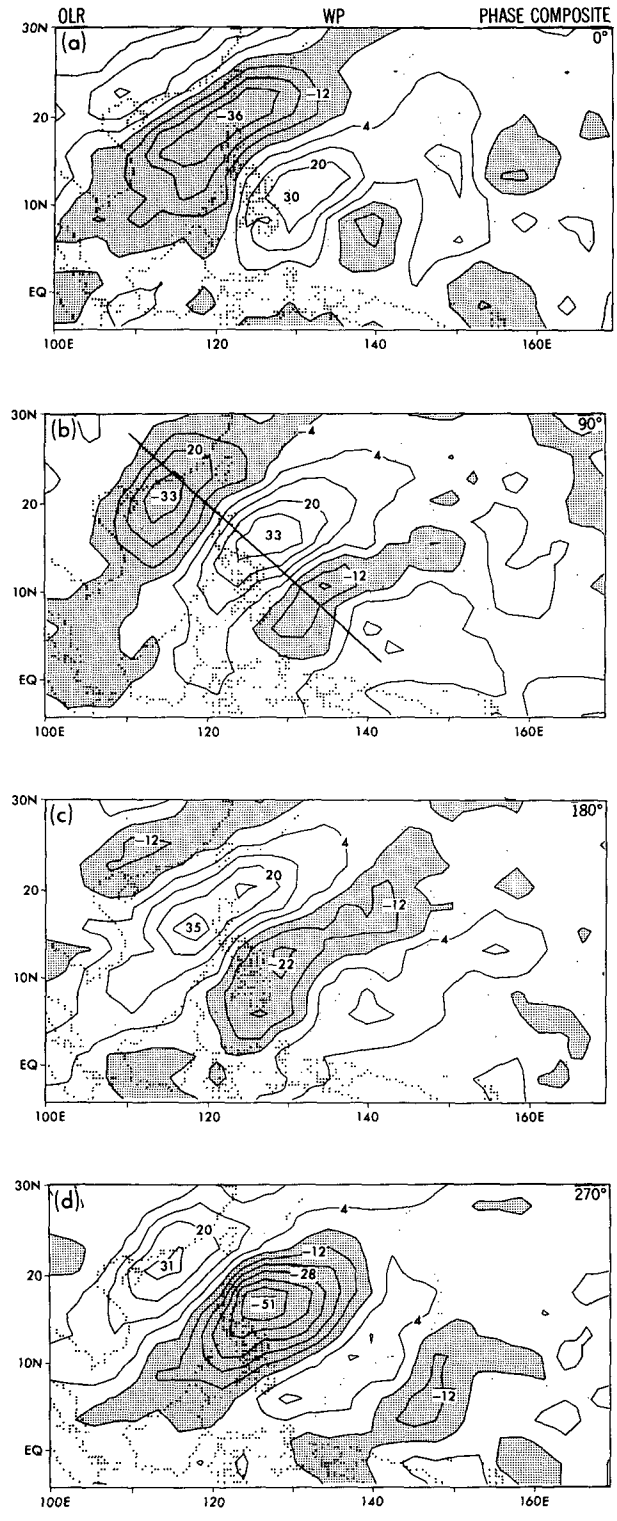

FIG. 14. Distributions of the composite patterns of bandpass-filtered outgoing longwave radiation fluctuations associated with the WP mode, as constructed on the basis of the REEOF coefficients. The four panels (a)–(d) show the results at phases 0°, 90°, 180° and 270°, respectively. Contour labels are in units of W m^{-2}, and contour interval is 8 W m^{-2}. Values less than −4 W m^{-2} are stippled. Refer to text for details of the composite procedure.

perturbations of pressure velocity attain dual extrema at 300 and 850 mb. This characteristic has been reported independently by Reed et al. (1977) for the African easterly waves using observations during GATE, and also by Nitta and Takayabu (1985) using FGGE data. Comparison between Figs. 16a and 16c indicates the occurrence of maximum upward motion at 850 mb (and hence near-surface convergence) near the low level trough. At the 200–300 mb level, the upward motion tends to lag positive ζ fluctuations by about one-eighth of a wavelength. This phase relationship may be interpreted using the simplified barotropic vorticity equation:

$$f\frac{\partial\omega}{\partial p} \approx \frac{\partial\zeta}{\partial t} + \mathbf{V}\cdot\nabla(\zeta + f).$$

Assuming that the beta-effect is small in synoptic scale motion, and that the wavelike systems propagate with a characteristics phase velocity $\mathbf{c}$, we then have

$$f\frac{\partial\omega}{\partial p} \approx \mathbf{V}_r\cdot\nabla\zeta$$

where $\mathbf{V}_r = \mathbf{V} - \mathbf{c}$ is the velocity relative to the propagating wave. Differentiation with respect to pressure yields

$$f\frac{\partial^2\omega}{\partial p^2} \approx \frac{\partial}{\partial p}(\mathbf{V}_r\cdot\nabla\zeta).$$

Assuming wavelike dependence of ω on p, we require that

$$-\omega \propto -\frac{\partial}{\partial p}(-\mathbf{V}_r\cdot\nabla\zeta);$$

i.e., increasing vorticity advection with height is accompanied by rising motion (see similar deduction by Holton 1979, pp. 136–143). For a mean flow which is easterly relative to the propagation speed, the advection term $(-\mathbf{V}_r\cdot\nabla\zeta)$ attains maximum and minimum values to the west and east of the troughs, respectively. Since ζ perturbations for the tropical disturbances are confined to the lower troposphere (see Fig. 16a), $-\partial(-\mathbf{V}_r\cdot\nabla\zeta)/\partial p$ would be negative (positive) to the west (east) of the troughs, and hence sinking (rising) motion would prevail in the middle and upper troposphere ahead (behind) the troughs, as shown in Fig. 16c. If the relative mean flow is westerly at the lower level, the reverse situation (i.e., rising motion to the west of the trough and sinking motion to the east) would be anticipated.

Temperature perturbations (Figs. 15e and 16d) have typical amplitudes of less than 1°C. The most notable features in the temperature vertical cross-section are the extrema at 300 mb. These warm and cold centers are located directly above the low level troughs and ridges, respectively. The warm center is probably associated with condensational heating accompanying

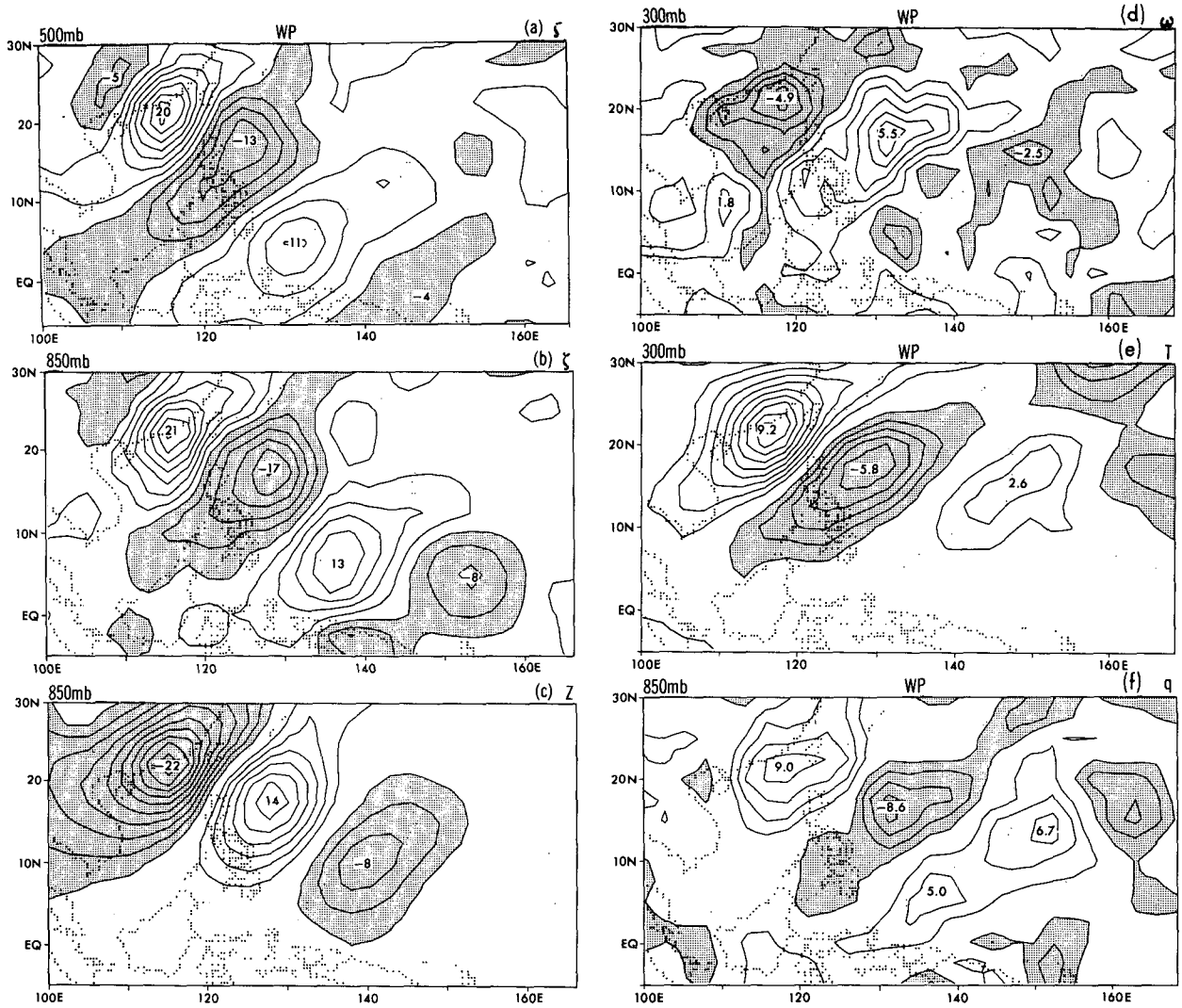

FIG. 15. Distributions of the composite patterns of bandpass-filtered (a) 500 mb relative vorticity, (b) 850 mb relative vorticity, (c) 850 mb geopotential height, (d) 300 mb pressure velocity, (e) 300 mb temperature and (f) 850 mb specific humidity, associated with a given phase (90°) of the WP disturbances. Contour intervals for panels (a)–(f) are 3×10^{-6} s^{-1}, 3×10^{-6} s^{-1}, 2 gpm, 1×10^{-2} Pa s^{-1}, 0.1°C, and 2×10^{-4}, respectively. Stippling in the respective panels indicates negative values less than -1.5×10^{-6} s^{-1}, -1.5×10^{-6} s^{-1}, -2 gpm, -0.5×10^{-2} Pa s^{-1}, -0.1°C, and -2×10^{-4}. The zero contours are omitted.

the low level convergence. This interpretation is supported by the almost 180° out-of-phase relationship between the OLR and 300 mb temperature anomalies (Figs. 14b and 15e). Also apparent in Fig. 16d is a shallow cold center extending from the surface to 700 mb, and lagging behind the low level trough.

Moist and dry centers appearing in the patterns for specific humidity (Figs. 15f and 16e) tend to lag behind the 850 mb trough and ridges, respectively, by about one-eighth of a wavelength. Behind the wave trough, the prevalent southeasterly trades is strengthened by the perturbation southeasterly inflow towards the trough. This effect may increase the surface evaporation and contribute to the moistening of the lower troposphere behind the trough. Analogously, the negative humidity fluctuation ahead of the trough could be caused by suppressed surface evaporation due to cancellation among the perturbation northwesterly inflow and the prevalent southeasterly trades. Another contributing factor to the phase relationship between the perturbations in ζ and specific humidity is the positive advection of water vapor by the southerly flow behind the wave trough, and the negative advection by the northerly flow ahead of it.

To study the relation between the transients and the ambient large-scale flows, we have composited the average flow condition when the WP mode is active. This is done by first constructing the eight phase composites of a complete cycle using unfiltered wind data, and then performing an average over all eight composites.

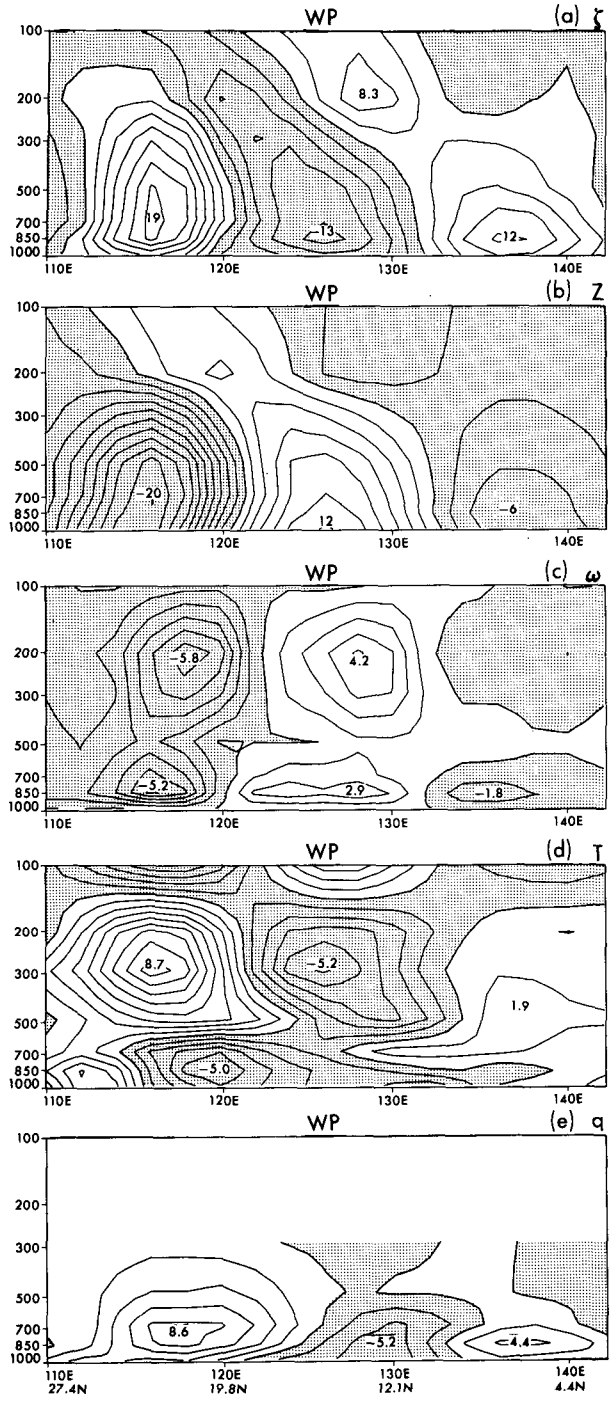

FIG. 16. Vertical cross-sections of the composites of (a) relative vorticity, (b) geopotential height, (c) pressure velocity, (d) temperature and (e) specific humidity, corresponding to a given phase (90°) of the WP perturbations. The abscissa corresponds to a baseline (shown as a bold straight line segment in Fig. 14b) extending northwestward from 2.5°N, 142.5°E at the extreme right to 27.5°N, 110.0°E at the extreme left. The latitudes and longitudes of the selected points along the abscissa are given below panel (e). Only the longitudes are shown under the other panels. An analogous labeling scheme is used for Figs. 20 and 23. Contour intervals for panels (a)–(e) are 3×10^{-6} s^{-1}, 2 gpm, 1×10^{-2} Pa s^{-1}, 0.1°C, and 2×10^{-4}, respectively. Stippling indicates negative values.

We shall denote this average as the WP *mode mean flow condition.* The climatological circulation pattern, as computed using all available data for the summers of 1980–1987, and the WP mode mean flow condition, are shown in Figs. 17a and 17b, respectively. The difference between these two patterns is displayed in Fig. 17c. It is found that the WP transients occur in conjunction with strengthening and westward protrusion of the subtropical anticyclone in the western Pacific, with the average southeasterly current towards the south China coast being approximately twice as strong as its climatological counterpart.

The closed contours in Fig. 17b depict the rms of the eight individual WP phase composites of bandpass-filtered 850 mb ζ data. It is evident that the most active transient activity is located to the southeast of the mean easterly maximum. The concurrent changes in both the level of synoptic activity and the ambient flow field are suggestive of considerable dynamical interactions among the high- and low-frequency components of the circulation over the western Pacific. One of these modes of interaction is the local barotropic energy conversion from the mean flow to the transient eddies, as is pointed out earlier in section 4 regarding the characteristic horizontal phase tilt of the disturbances, and their placement in the shear zone of the southeasterly background flow.

b. Indian mode

The mean flow structure in which the disturbances associated with the Indian (IN) mode are embedded is illustrated in Fig. 18. Similar to Fig. 17b, this pattern has been computed by averaging the eight individual phase composites of unfiltered 850 mb wind field for the IN mode. There are evidently substantial differences between the ambient circulation for the IN mode and that in the WP sector. The pattern in Fig. 18 is dominated by a strong westerly monsoon flow extending eastward from the Somali coast to the South China Sea. The westerly current shown here is slightly (~2 m s^{-1}) stronger than the climatological mean. From the distribution of the rms of the eight phase composites of bandpass-filtered 850 mb ζ (closed contours in Fig. 18), it is apparent that the most active transients develop on the northern side of the low-level monsoon current.

To illustrate the convective activity associated with the IN mode, we show in Fig. 19 the composite of the OLR data for one particular phase of the cycle. A large negative OLR perturbation is seen over the Bay of Bengal, while a positive center is located over western India. The series of composite charts for successive phases (not shown) indicate that the disturbances are rather weak when they make their first appearance near 5°–10°N, 110°E, but substantial growth takes place as they propagate west-northwestward towards northwestern India. The disturbances in the Indian sector

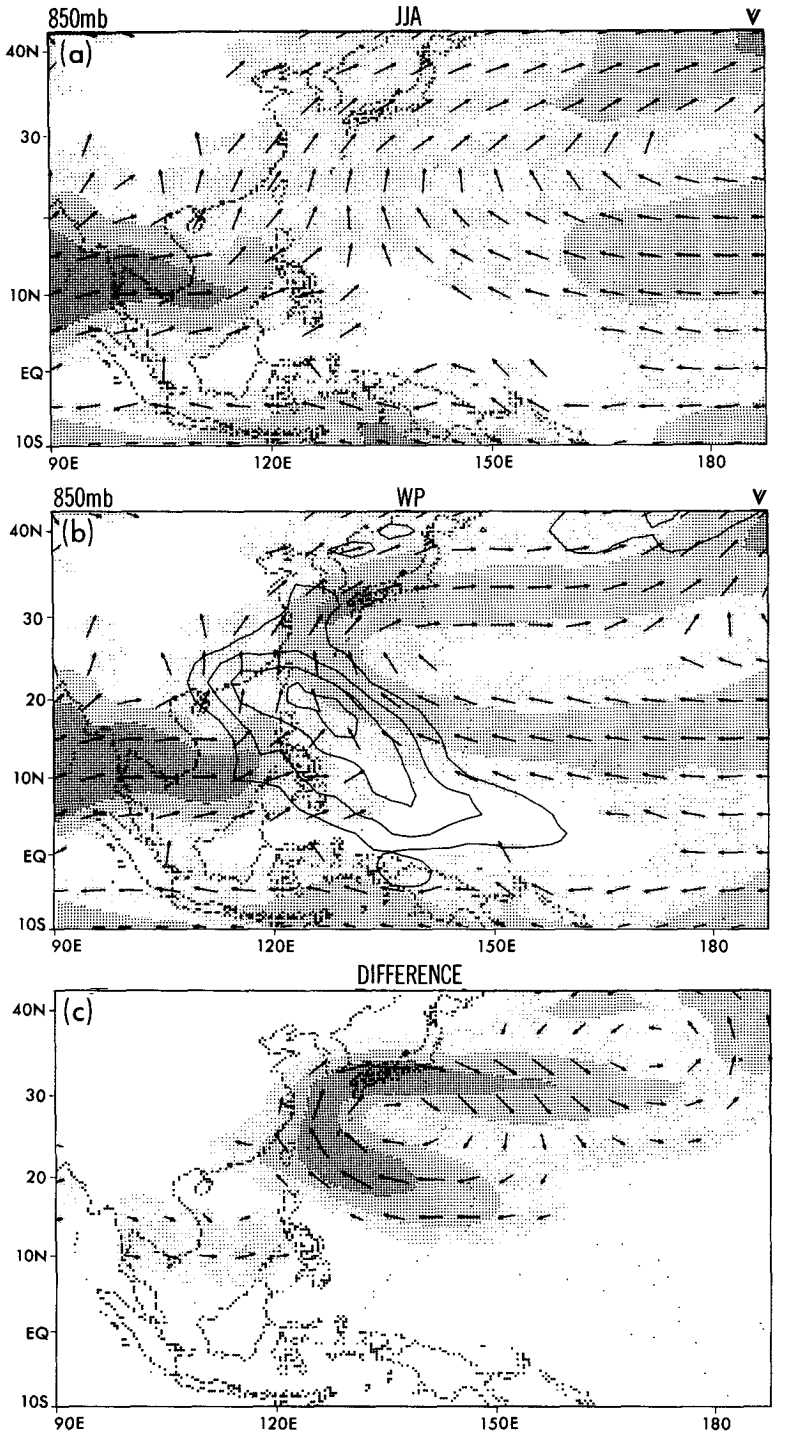

FIG. 17. (a) Distribution of the 850 mb horizontal wind in the western Pacific, as averaged over eight summers. Light stippling is for wind speeds between 2–5 m s^{-1}, medium stippling for 5–8 m s^{-1}, and dense stippling for speeds larger than 8 m s^{-1}. Wind speeds less than 2 m s^{-1} are not stippled, and the corresponding directional arrows are not shown. (b) Similar to (a), but averaged only over time intervals when WP disturbances are active. The closed contours indicate the distribution of the rms of the phase composites of bandpass-filtered 850 mb vorticity for a complete cycle of the WP mode. Contour interval is 3×10^{-6} s^{-1}. The first isoline corresponds to a value of 4×10^{-6} s^{-1}. (c) Difference between the vector wind fields in (b) and (a). The light, medium, and dense stippling indicate differences of 1–2 m s^{-1}, 2–3 m s^{-1}, and larger than 3 m s^{-1}, respectively. In panel (c), the length of the arrows is scaled according to the differences in wind speeds. Values less that 1 m s^{-1} are not stippled, and the corresponding arrows are omitted.

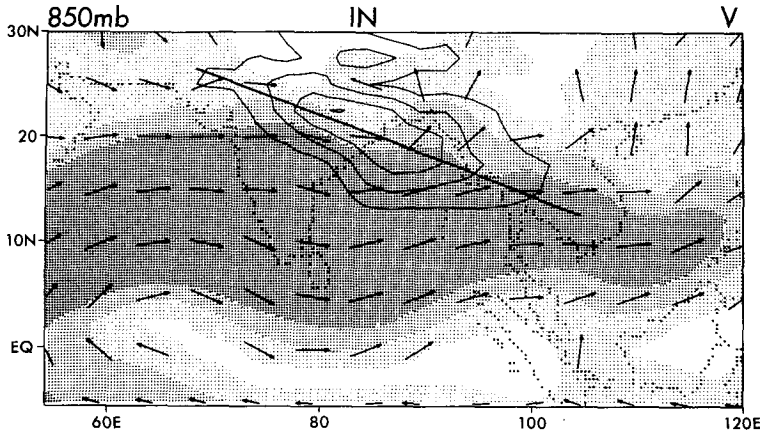

FIG. 18. Similar to Fig. 17b, but for the Indian region, and obtained for time intervals when IN disturbances are active. The closed contours depict the distribution of rms associated with the eight phase composites of bandpass-filtered 850 mb vorticity perturbations of the IN mode.

generally acquire a less wavelike character as compared to the features associated with the WP mode.

The vertical cross-sections of the composites of different variables for a given phase of the IN mode are shown in Fig. 20. The abscissa in these diagrams extends from 26.4°N, 70°E at the left to 13.6°N, 105°E at the right, and coincides with the more active portion of the propagation path for disturbances associated with this mode (see bold line in Fig. 18). As in the WP disturbances, the amplitudes of ζ and geopotential height for the IN perturbations are strongest at 850–700 mb, and decrease with height in the middle and upper troposphere. The ridge and trough axes exhibit a northwestward phase tilt with height above 700 mb. However, the panel for geopotential height (Fig. 20b) indicates that a southeastward tilt prevails below 700 mb.

Similar to the WP mode, dual extrema in the lower and upper troposphere are found in the vertical cross-section for ω (Fig. 20c). However, in contrast to the WP mode, the upper-level upward (downward) motion is found to the west of the lower level trough (ridge) in the IN mode. As noted in the last subsection, this phase relation may be interpreted as a result of the differential relative vorticity advection with a low-level westerly (instead of easterly) mean flow relative to the propagating disturbance.

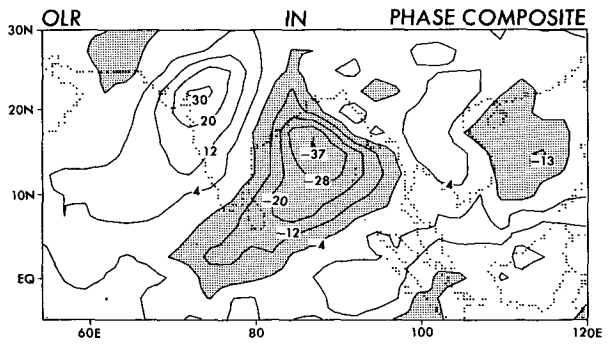

FIG. 19. Distribution of the composite pattern for bandpass-filtered outgoing longwave radiation for a given phase of the IN disturbances. Contour labels are in units of W m^{-2}, and contour interval is 8 W m^{-2}. Values less than −4 W m^{-2} are stippled.

For temperature perturbations, a warm (cold) center develops in the 200–300 mb layer directly above the 850 mb trough (ridge). Similar to the WP mode, these upper-level temperature perturbations appear to be related to convective activity, as they are almost exactly out of phase with the OLR perturbations (not shown). Near the surface, there is a warm (cold) center situated ahead (behind) of the wave trough, implying a net southward eddy heat transport at the surface. Noting that the continental area around the Tibetan Plateau is warmer than the equatorial Indian Ocean during the summer months, this transport is directed down the average surface temperature gradient.

Contrary to the situation in the WP mode, the humidity perturbations are seen to lead (rather than lag) the corresponding ζ fluctuations by about one-eighth of a wavelength (Fig. 20e). This relationship may be partially explained by the respective enhancement and suppression of evaporation west and east of the troughs by the combined effect of perturbation inflow and mean monsoon westerlies [see discussion of the humidity composite (Fig. 16e) in the last subsection].

c. Atlantic mode

It is well known that easterly waves in the Atlantic sector are related to the midtropospheric easterly current at around 600–700 mb. In Fig. 21 is shown the average of eight individual phase composites of the 700 mb wind associated with the AT mode. Easterlies are seen to prevail throughout this region. An enhanced

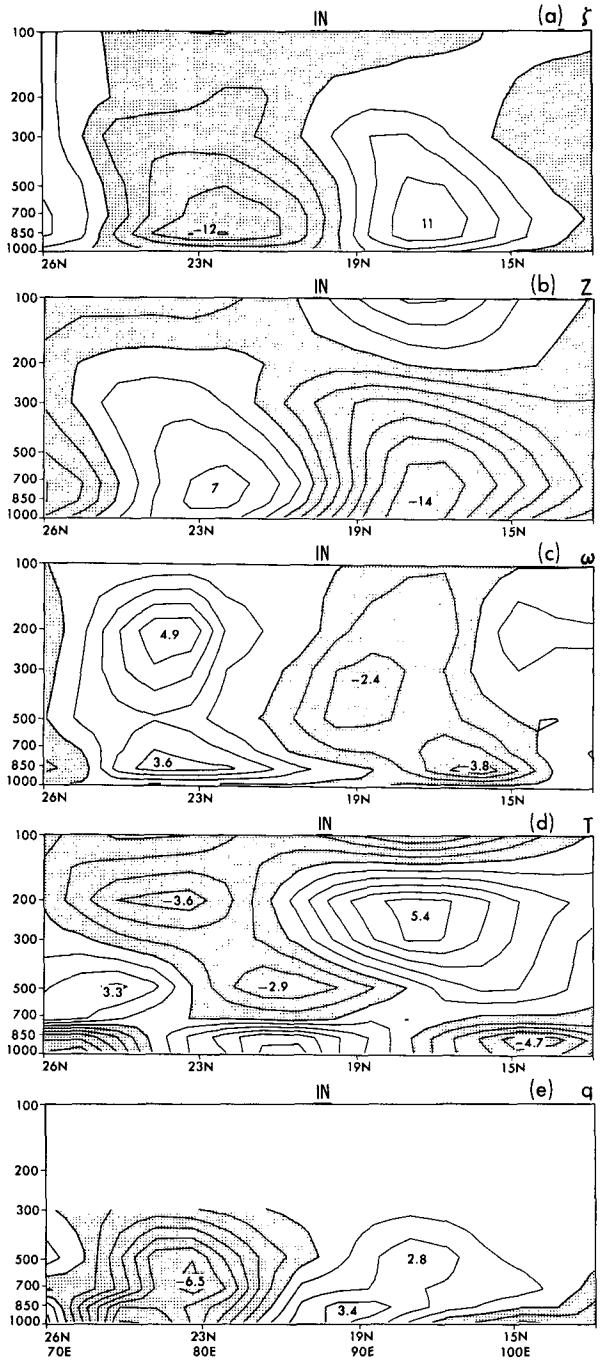

FIG. 20. Similar to Fig. 16, but for IN disturbances in the Indian region. The abscissa corresponds to a baseline (shown as a bold straight line segment in Fig. 18) extending northwestward from 13.6°N, 105°E at the extreme right to 26.4°N, 70°E at the extreme left.

easterly current originates at about 10°–15°E and extends towards the Atlantic along 15°N. This current is collocated with the strong latitudinal temperature gradient south of the Sahara region.

The distribution of the rms of the eight individual phase composites of 700 mb ζ, as depicted by the contour lines in Fig. 21, reveals two elongated regions of enhanced transient activity. One of these active zones extends from 0°W to 70°W at 5°–10°N. The other, stronger region of activity spans westward from northern Africa to the Gulf of Mexico at 15°–20°N. Our EEOF analysis, hence, substantiates the finding by a number of earlier researchers (e.g., Carlson 1969a, 1969b; Burpee 1972, 1974; Reed et al. (1988a,b) that two preferred tracks exist in the African/Atlantic sector.

The horizontal structure of disturbances associated with the AT mode is illustrated by composite patterns of (a) 700 mb ζ, (b) OLR, and (c) 850 mb temperature for a given phase in Fig. 22. The amplitudes of perturbations in the ζ and OLR composites are weaker than those associated with the WP or IN modes. Extrema of the 700 mb ζ perturbation are seen along the two axes of enhanced variance shown in Fig. 21. The disturbances acquire a southwest to northeast tilt to the south of the midtropospheric easterly current, and a northwest to southeast tilt farther north, thus, implying a local barotropic transfer of kinetic energy from the mean flow to the eddies. The characteristic horizontal tilt north of the midtropospheric current is no longer evident over the Atlantic. Over continental Africa, the OLR perturbations are weak (Fig.22b). Convective activity appears to be better organized over the Atlantic, and the OLR centers coincide the 700 mb troughs and ridges.

Vertical cross-sections of the AT disturbances along the southern axis of maximum variance near 7.5°N (not shown), as well as horizontal patterns of various fields indicate that the structure of these disturbances is similar to (but weaker than) those associated with the WP mode. The present discussion on the vertical structure of the AT mode will be focused on the northern track, where significant differences from the WP mode can be identified along the portion within continental Africa. Figure 23 shows the vertical cross-sections of phase composites for the AT mode along the northern track from 22.5°N, 90°W to 17.5°N, 20°E. The location of this track is depicted by the bold line in Fig. 22a. From Fig. 23, it is evident that the disturbance undergo substantial changes as they cross the west African coast into the Atlantic. Hence, we shall refer to the disturbances situated east and west of 20°W as the *continental* and *oceanic* perturbations, respectively.

The patterns in Fig. 23 indicate a general westward tilt with height for ζ and geopotential perturbations above 500 mb. The geopotential fluctuations in the continental sector exhibit a slight eastward tilt with height in the lower troposphere. The continental perturbations are strongest at the lower levels, with maximum amplitudes being located at the surface or 850 mb. Over oceanic areas, the level of strongest perturbations is raised to 700 mb. The perturbations near the tropopause strengthen as they propagate westward

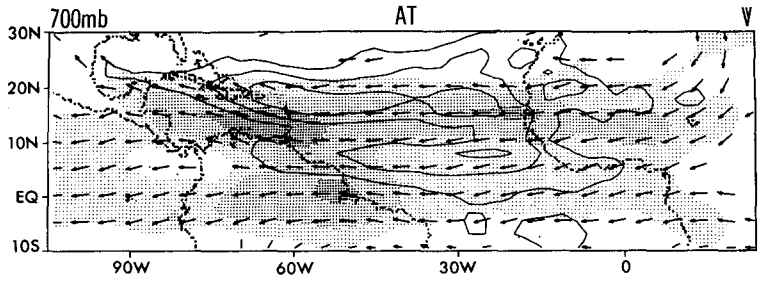

FIG. 21. Distribution of the horizontal wind at 700 mb, as averaged over the time periods when the AT disturbances are active. Light stippling is used for values between 5–7 m s^{-1}, medium stippling for 7–9 m s^{-1}, and dense stippling for speeds larger than 9 m s^{-1}. The directional arrows are not shown for speeds less than 3 m s^{-1}, and values less than 5 m s^{-1} are not stippled. The closed contours indicate the distribution of the rms of the eight composites of bandpass-filtered 700 mb relative vorticity perturbations associated with the AT mode. Contour interval is 1.5×10^{-6} s^{-1}. The first contour corresponds to values of 2×10^{-6} s^{-1}.

into the Atlantic, so that secondary extrema appear at 200 mb to the west of 40°W. The intensification of upper level perturbations in mid-Atlantic has been noted by many researchers, and is considered to be a result of the interaction between the semipermanent upper-level trough and low-level synoptic scale disturbances (Reed et al. 1988b). At about 60°W, the AT mode disturbances start to weaken as they take a more west-northwestward course into the Caribbean (Fig. 22).

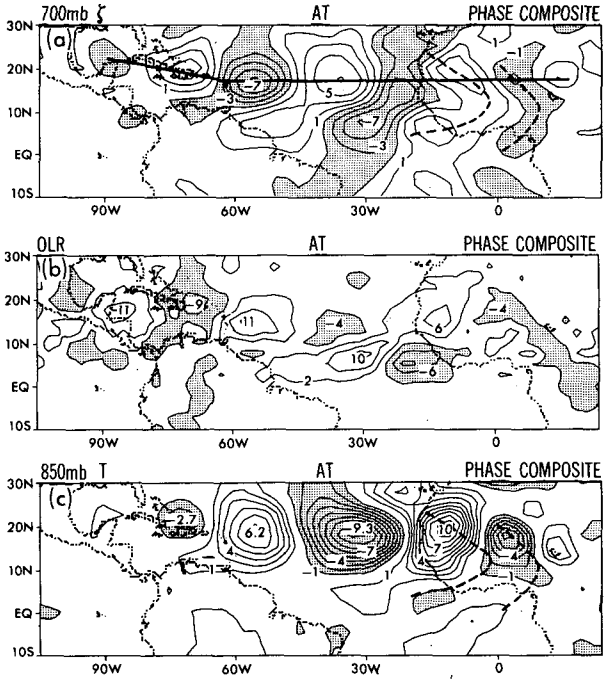

FIG. 22. Distributions of the composite patterns of (a) 700 mb relative vorticity, (b) outgoing longwave radiation, (c) 850 mb temperature, for a given phase of the AT fluctuations. Contour intervals for panels (a)–(c) are 2×10^{-6} s^{-1}, 4 W m^{-2}, and 0.1°C, respectively. Stippling in the respective panels indicates negative values less than -1×10^{-6} s^{-1}, -2 W m^{-2}, and -0.1°C. Zero contours are omitted. Over continental western Africa, two dashed lines are drawn in panels (a) and (c) to show the locations of the 700 mb trough and ridge axes.

Over the continent, the upper level vertical motions are relatively weak, and maximum ω perturbations are found at 700–850 mb. West of 40°W, the strongest vertical motions appear at 300–500 mb (Fig. 23c), with rising motion lagging behind the lower level wave trough. This relationship is similar to that noted in the WP mode. In contrast to the WP and IN modes, no dual ω extrema are found anywhere along the northern track. Dual ω extrema are found along the southern track.

Unlike other variables, the temperature perturbations of the continental African waves (Figs. 22c and 23d) are stronger than those associated with the western Pacific and the Indian disturbances. Maximum temperature fluctuations occur in the lower troposphere. Comparisons among the five panels of Fig. 23 reveal that surface troughs in the continental sector occur in conjunction with ascent of warm and dry air, whereas descent of cold and moist air prevails over surface ridges. This characteristic thermal-low structure was noted earlier by Burpee (1974) when he analyzed northern African wave disturbances at 20°N. As in the western Pacific, the surface troughs and ridges in the Atlantic are accompanied by cold and warm temperature perturbations in the lower troposphere, respectively; whereas the moist and dry centers lag the low-level troughs and ridges by almost a quarter wavelength.

Finally, we note that the horizontal temperature structure near 10°N is rather different from that along the northern track. To highlight such differences, two dash lines are plotted in Figs. 22a and 22c to illustrate the location of the continental trough and ridge axes at 700 mb. We see that the 850 mb temperature fluctuations lead the 700 mb vorticity perturbations only slightly at 20°N, but by as much as a quarter wave-

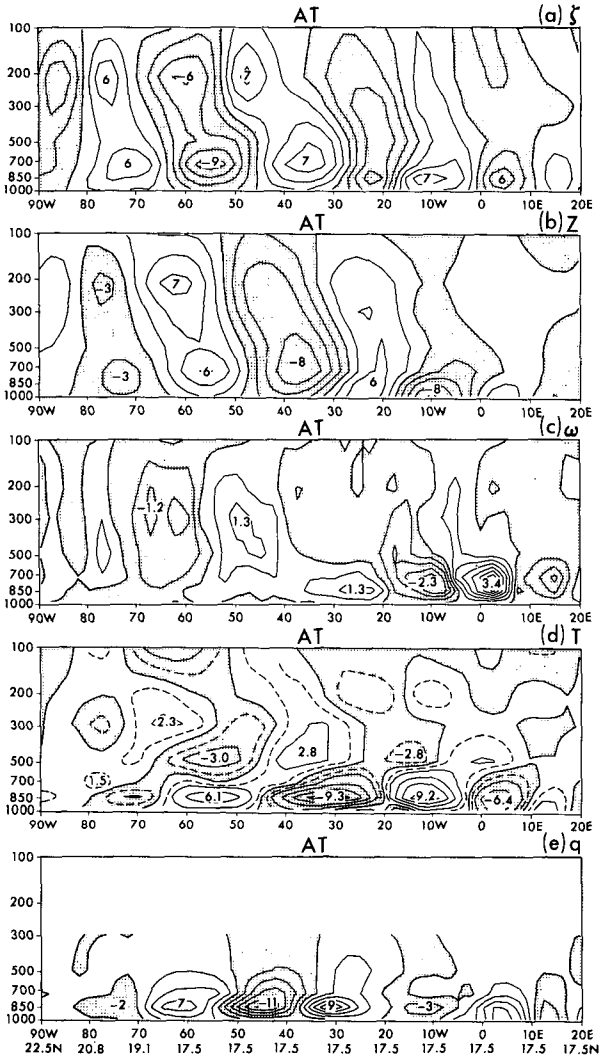

FIG. 23. Vertical cross-sections of the composite of (a) relative vorticity, (b) geopotential height, (c) vertical pressure velocity, (d) temperature and (e) specific humidity, corresponding to a given phase of the AT fluctuations. The abscissa corresponds to the bold baseline shown in Fig. 22a, which extends from 17.5°N, 20°E at the extreme right to 22.5°N, 90°W at the extreme left. Contour intervals for panels (a)–(e) are 2×10^{-6} s^{-1}, 2 gpm, 5×10^{-3} Pa s^{-1}, 0.2°C and 2×10^{-4}, respectively. Dashed contours for values of 0.1 and −0.1°C are added in panel (d). Stippling indicates negative values.

length near 10°N. The former phase difference is largely a result of the eastward tilt with height of vorticity perturbations from 850 to 700 mb, so that the temperature and vorticity perturbations are actually more or less in phase at 850 mb (see Figs. 23a and 23d). The much more noticeable phase shift near 10°N persists even for temperature and vorticity perturbations at the same level.

7. Summary and discussion

This study demonstrates that a considerable amount of useful information on the behavior of tropical circulation systems may be extracted from the global four-dimensional assimilation products currently generated at operational weather centers. With the ECMWF analyses, we have documented the preferred locations, three-dimensional structure, and propagation characteristics of tropical synoptic-scale summertime disturbances. Enhanced variability of the 850 mb ζ field has been noted over western Africa, the eastern and the western subtropical Pacific, and the Bay of Bengal/northern Indian regions. The power spectra of 850 mb ζ in these regions exhibit pronounced peaks at periods shorter than ten days. Such characteristic periods range from 3–5 days in western Africa, to 5–6 days in the eastern Pacific, and 6–9 days in the western Pacific and Indian regions. There is some evidence that the dominant period varies gradually even within a given active region, with longer periods towards the northwestern end of each region.

We have also shown that the lag-correlation techniques introduced by Wallace et al. (1988) in their study of midlatitude cyclones are quite applicable to the diagnosis of tropical transient activities using global gridded analyses. We find that normalized measures such as teleconnectivity or temporal coherence are useful tools for depicting small amplitude but organized tropical disturbances. These measures yield information which is not evident from the distribution of rms statistics alone. The products of the lag-correlation analysis collectively offer a concise description of the typical horizontal structure, temporal evolution, and growth/decay behavior of the tropical disturbances. It is seen that a substantial amount of synoptic-scale variability in the active regions within the tropical belt is associated with westward traveling wavelike features. The properties of these features as deduced in this study are in agreement with previous synoptic investigations of such phenomena.

We have also conducted a survey of the transient activities throughout the tropical belt by using EEOF/REEOF techniques. Active transient disturbances are identified at the same sites as those inferred from the lag-correlation analyses. Subsequently, an EEOF/REEOF composite method has been used to depict the vertical and horizontal structure of the tropical transients in the western Pacific, the Bay of Bengal/northwestern India, and the western African/Atlantic/Carribbean regions. Strongest vorticity perturbations are found in the lower troposphere for all tropical transients. It is also noted that the horizontal phase tilt and the placement of the transients with respect to the mean-flow shear generally indicate kinetic energy transfer from the mean flow to the eddies. There are substantial variations in the phase relationships among different variables for tropical wave modes at various locations. Much of this geographical dependence can be attributed to changes in the mean atmospheric condition in which the disturbances are embedded. In particular, the relationship between the fluctuations in vorticity and vertical motion may be interpreted in terms of the differential relative vorticity advection by

the prevalent background flow. Similarly, the modulation of surface evaporation by the combined effect of the surface mean circulation and the perturbation inflow or outflow seem to exert a considerable influence on the displacement of the specific humidity fluctuations from the maritime vorticity centers.

The composite analysis for the AT mode reveals two preferred paths of propagation in the western African region. As shown by Burpee (1974), the transient activity along the stronger northern track at 20°N acquires many of the characteristics typical for desert-type disturbances, with dry, warm rising air above the troughs, and relatively moist, cool sinking air at the ridges. These disturbances are not associated with any prominent signal in the OLR composites. The southern track is located near a zonally elongated region of maximum rainfall at around 10°N. Similar to the results presented by Reed et al. (1977), the thermal structure of the disturbances in this region is similar to that associated with maritime disturbances. In particular, lower level cold centers and upper level warm centers are typically found above the near-surface troughs. Moreover, these disturbances are accompanied by better organized OLR perturbations. The coincidence of negative OLR fluctuations with the upper-level warm centers suggests that organized convection and latent heating may contribute to the maintenance of these disturbances.

Our understanding of the dynamical processes that are responsible for the formation, maintenance, and decay of synoptic scale disturbances is still incomplete. Norquist et al. (1977) studied the energy budget of the African waves and found that baroclinic and barotropic processes contribute almost equally to the disturbances. They also concluded tentatively that latent heating and convective processes are important for African distrubances occurring near the summertime rainfall maximum. With the availability of the ECMWF analyses, similar budget analyses may be repeated for the African disturbances, as well as for the wave modes in other regions. Such calculations should ascertain the role of various dynamical and physical mechanisms in the eddy development at different sites.

The sites of active transient activity identified in this study are well known for their abundance of vortex-like weather systems in the summer (e.g., monsoon depressions in the Bay of Bengal and typhoons in the western Pacific). Elsberry et al. (1987) noted that these systems often occur in succession within active periods of about 2–3 weeks. It is conceivable that some of them may develop from strong episodes of the wavy disturbances documented in this study. Further diagnosis is evidently needed to clarify the relationships between the wavelike transients and the intense cyclonic vortices in the tropics.

Furthermore, Lau et al. (1989) noted that westward propagating disturbances could form as a result of atmospheric adjustment processes accompanying the penetration of the eastward propagating 40–50 day oscillations into the strong convective zone over the western Pacific. The 40–50 day oscillations have also been suggested as having a modulating effect for typhoon activity in the western Pacific (Elsberry et al. 1987). It would, therefore, be of interest to explore the link between the high-frequency perturbations examined here and other more slowly varying tropical phenomena. Studies on the interactions between the synoptic scale transients and other components of the atmospheric circulation in the tropics are limited, probably due to the earlier lack of an adequate observational database, and the difficulties in identifying transient features of different time scales. We believe that the temporal coefficients of the EEOFs/REEOFs (section 6) provide a convenient basis for examining various circulation features of interest, as well as their mutual interactions.

A better description of the transient structure in different areas should facilitate modeling efforts aimed at understanding such tropical phenomena. It is apparent from earlier African wave simulations [Holton (1971); Mass (1979); and Shapiro et al. (1988)] that multilayer linear models are capable of generating instability modes that resemble the observed wave structure. Analogous experiments with prescribed mean flow conditions corresponding to other active sites should be helpful for evaluating the relative importance of various mechanisms in determining the three-dimensional structure as well as the genesis and maintenance of these tropical transients. It is also noteworthy that typhoon activity has been reported to occur in simulations with comprehensive general circulation models (Broccoli and Manabe, personal communication). Using the methods presented in this study, the tropical transient behavior in these models can be analyzed readily. It would be of interest to study the interactions between the synoptic scale waves and tropical vortices appearing in the model atmosphere.

Acknowledgments. We would like to thank A. H. Oort and A. J. Broccoli for reading the manuscript and offering helpful comments. The valuable suggestions from B. Liebmann, R. J. Reed, L. J. Shapiro and an anonymous reviewer are also appreciated. The OLR dataset was furnished by K.-M. Lau, and the ROHK analyses were made available to us courtesy of E. Koo and C. Y. Lam. The figures were prepared by the Scientific illustration Group at GFDL and J. Conner. The research of KHL was supported by NSF Grant ATM-8218761 and by the NOAA Equatorial Pacific Ocean Climate Studies Program through Grant NA87EAD00039.

REFERENCES

Bengtsson, L., M. Kanamitsu, P. Kallberg and S. Uppala, 1982: FGGE 4-dimensional data assimilation at ECMWF. *Bull. Amer. Meteor. Soc.*, **63**, 29–43.

Blackmon, M. L., 1976: A climatological spectral study of the 500 mb geopotential height of the Northern Hemisphere. *J. Atmos. Sci.*, **33**, 1607–1623.

——, Y.-H. Lee and J. M. Wallace, 1984a: Horizontal structure of 500 mb height fluctuations with long, intermediate and short time scales. *J. Atmos. Sci.*, **41**, 961–979.

——, J. M. Wallace, N.-C. Lau and S. L. Mullen, 1977: An observational study of the Northern Hemisphere wintertime circulation. *J. Atmos. Sci.*, **34**, 1040–1053.

——, Y.-H. Lee and J. M. Wallace, and H.-H. Hsu, 1984b: Time variation of 500 mb height fluctuation with long, intermediate, and short time scales as deduced from lag-correlation statistics. *J. Atmos. Sci.*, **41**, 981–991.

Burpee, R. W., 1972: The origin and structure of easterly waves in the lower troposphere of north Africa. *J. Atmos. Sci.*, **29**, 77–90.

——, 1974: Characteristics of north African easterly waves during the summers of 1968 and 1969. *J. Atmos. Sci.*, **31**, 1556–1570.

Carlson, T. N., 1969a: Synoptic histories of three African disturbances that developed into Atlantic hurricanes. *Mon. Wea. Rev.*, **97**, 256–276.

——, 1969b: Some remarks on African disturbances and their progress over the tropical Atlantic. *Mon. Wea. Rev.*, **97**, 716–726.

Chang C.-P., V. F. Morris and J. M. Wallace, 1970: A statistical study of easterly waves in the western Pacific: July–December 1964. *J. Atmos. Sci.*, **27**, 195–201.

Charney, J. G., and M. E. Stern, 1962: On the stability of internal baroclinic jets in a rotating atmosphere. *J. Atmos. Sci.*, **19**, 159–172.

Elsberry, R. L., W. M. Frank, G. J. Holland, J. D. Jarrell and R. L. Southern, 1987: *A Global View of Tropical Cyclone.* University of Chicago Press, 1985 pp. [Chapter 3, Tropical cyclone formation, page 67.]

Hartmann D. L., and M. L. Michelsen, 1989: Intraseasonal periodicities in Indian rainfall. *J. Atmos. Sci.*, **46**, 2838–2862.

Hollingsworth, A., D. B. Shaw, P. Lonnberg, L. Illari, K. Arpe and A. J. Simmons, 1986: Monitoring of observation and analysis quality by a data assimilation system. *Mon. Wea. Rev.*, **114**, 861–879.

Holton, J. R., 1971: A diagnostic model for equatorial wave disturbances: The role of vertical shear of the mean zonal wind. *J. Atmos. Sci.*, **28**, 55–64.

Kuo, H. L., 1949: Dynamic instability of two-dimensional non-divergent flow in a barotropic atmosphere. *J. Meteor.*, **6**, 105–122.

Kutzbach, J. E., 1967: Empirical eigenvectors of sea level pressure, surface temperature and precipitating complexes over North America. *J. Appl. Meteor.*, **6**, 791–802.

Lau, K. M., Li Peng, C. H. Sui and T. Nakazawa, 1989: Dynamics of super cloud clusters, westerly wind bursts, 30–60 day oscillations and ENSO: An unified view. *J. Meteorol. Soc. Jpn.*, **67**, 205–219.

Liebmann B., and H. H. Hendon, 1990: Synoptic-scale disturbances near the equator. *J. Atmos. Sci.*, **47**, 1463–1479.

Mass, C., 1979: A linear primitive equation model of African wave disturbances. *J. Atmos. Sci.*, **36**, 2075–2092.

Nitta, T., and Y. Takayabu, 1985: Global analysis of the lower tropospheric disturbances in the tropics during the northern summer of the FGGE year. Part II: Regional characteristics of the disturbances. *Pure Appl. Geophys.*, **123**, 272–292.

——, Y. Nakagomi, Y. Suzuki, N. Hasegawa and A. Kadokura, 1985: Global analysis of the lower tropospheric disturbances in the tropics during the northern summer of the FGGE year. Part I: Global features of the disturbances. *J. Meteorol. Soc. Jpn.*, **63**, 1–19.

Norquist, D. C., E. E. Recker and R. J. Reed, 1977: The energetics of African wave disturbances as observed during phase III of GATE. *Mon. Wea. Rev.*, **105**, 334–342.

North, G. R., T. L. Bell, R. F. Cahalan and F. J. Moeng, 1982: Sampling errors in the estimation of empirical orthogonal functions. *Mon. Wea. Rev.*, **110**, 699–706.

Piersig, W., 1936: Schwankungen von Luftdruck und Luftbewengung sowie ein Beitrag zum Wettergeschehen in Passatgebiet des ostlichen Nordatlantischen Ozeans. *Arch. Deut. Seewarte,* **54**(6). [Parts II and III have been translated and printed, 1944: The cyclonic disturbances of the subtropical eastern north Atlantic. *Bull. Amer. Meteor. Soc.*, **25**, 2–17.]

Reed, R. J., and E. E. Recker, 1971: Structure and properties of synoptic-scale wave disturbances in the equatorial western Pacific. *J. Atmos. Sci.*, **28**, 1117–1133.

——, D. C. Norquist, and E. E. Recker, 1977: The structure and properties of African wave disturbances as observed during phase III of GATE. *Mon. Wea. Rev.*, **105**, 317–333.

——, A. Hollingsworth, W. A. Heckley and F. Delsol, 1988a: An evaluation of the performance of the ECMWF operational forecasting system in analyzing and forecasting easterly wave disturbances over Africa and the tropical Atlantic. *Mon. Wea. Rev.*, **116**, 824–865.

——, E. Klinker and A. Hollingsworth, 1988b: The structure and characteristics of African easterly wave disturbances as determined from the ECMWF operational analysis/forecast system. *Meteor. Atmos. Phys.*, **38**, 22–33.

Regula, H., 1936: Druckschwankungen und tornados an der westkuste von Afrika. *Ann. Hydrogr. Mar. Meteor.*, **64**, 107–111. [Original quote from Burpee (1972, 1974).]

Richman, M. B., 1986: Rotation of principal components. *J. Climatol.*, **6**, 293–335.

Riehl, H., 1954: *Tropical Meteorology.* McGraw-Hill, 392 pp.

Shapiro, L. J., 1986: The three-dimensional structure of synoptic-scale disturbances over the tropical Atlantic. *Mon. Wea. Rev.*, **114**, 1876–1891.

——, D. E. Stevens and P. E. Ciesielski, 1988: A comparison of observed and model-derived structures of Caribbean easterly waves. *Mon. Wea. Rev.*, **116**, 921–938.

Simpson, R. H., N. Frank, D. Shideler and H. M. Johnson, 1969: Atlantic tropical disturbances of 1968. *Mon. Wea. Rev.*, **97**, 240–255.

Tai, K.-S., and Y. Ogura, 1987: An observational study of easterly waves over the eastern Pacific in the northern summer using FGGE data. *J. Atmos. Sci.*, **44**, 339–361.

Wallace, J. M., 1971: Spectral studies of tropospheric wave disturbances in the tropical western Pacific. *Rev. Geophys. Space Phys.*, **9**, 557–612.

——, and C.-P. Chang, 1969: Spectral analysis of large-scale wave disturbances in the tropical lower troposphere. *J. Atmos. Sci.*, **26**, 1010–1025.

——, and D. S. Gutzler, 1981: Teleconnections in the geopotential height field during the Northern Hemisphere winter. *Mon. Wea. Rev.*, **109**, 784–812.

——, G.-H. Lim and M. L. Blackmon, 1988: Relationship between cyclone tracks, anticyclone tracks and baroclinic waveguides. *J. Atmos. Sci.*, **45**, 439–462.

Weare, B. C., and J. S. Nasstrom, 1982: Examples of extended empirical orthogonal function analysis. *Mon. Wea. Rev.*, **110**, 481–485.

Yanai M., T. Maruyama, T. Nitta and Y. Hayashi, 1968: Power spectra of large-scale disturbances over the tropical Pacific. *J. Meteorol. Soc. Jpn.*, **46**, 308–323.

Zangvil, A., 1977: On the presentation and interpretation of spectra of large-scale disturbances. *Mon. Wea. Rev.*, **105**, 1469–1472.